Journal of Theoretical Biology 590 (2024) 111853

Contents lists available at ScienceDirect

Journal of Theoretical Biology

journal homepage: www.elsevier.com/locate/yjtbi

Flow modeling and structural characterization in fungal pellets ☆

J. Sánchez-Vargas [a,b], F.J. Valdés-Parada [c], L. Peraza-Reyes [d], D. Lasseux [e], M.A. Trujillo-Roldán [a,f,*]

[a] Departamento de Biología Molecular y Biotecnología, Instituto de Investigaciones Biomédicas, Universidad Nacional Autónoma de México, 04510, CDMX, Mexico
[b] Posgrado en Ciencias Bioquímicas, Universidad Nacional Autónoma de México, 04510, CDMX, Mexico
[c] División de Ciencias Básicas e Ingeniería, Universidad Autónoma Metropolitana-Iztapalapa, 09340, CDMX, Mexico
[d] Departamento de Bioquímica y Biología Estructural, Instituto de Fisiología Celular, Universidad Nacional Autónoma de México, 04510, CDMX, Mexico
[e] University of Bordeaux, CNRS, Bordeaux INP, I2M, UMR 5295, Bordeaux, F-33400, Talence, France
[f] Departamento de Bionanotecnología, Centro de Nanociencias y Nanotecnología, Universidad Nacional Autónoma de México, Ensenada, Baja California, Mexico

ARTICLE INFO

Keywords:
Fluid mechanics
Upscaling
Mathematical model
Laccaria trichodermophora

ABSTRACT

Fungal pellets are hierarchical systems that can be found in an ample variety of applications. Modeling transport phenomena in this type of systems is a challenging but necessary task to provide knowledge-based processes that improve the outcome of their biotechnological applications. In this work, an upscaled model for total mass and momentum transport in fungal pellets is implemented and analyzed, using elements of the volume averaging and adjoint homogenization methods departing from the governing equations at the microscale in the intracellular and extracellular phases. The biomass is assumed to be composed of a non-Newtonian fluid and the organelles impervious to momentum transport are modeled as a rigid solid phase. The upscaled equations contain effective-medium coefficients, which are predicted from the solution of adjoint closure problems in a three-dimensional periodic domains representative of the microstructure. The construction of these domains was performed for *Laccaria trichodermophora* based on observations of actual biological structures. The upscaled model was validated with direct numerical simulations in homogeneous portions of the pellets core. It is shown that no significant differences are observed when the dolipores are open or closed to fluid flow. By comparing the predictions of the average velocity in the extracellular phase resulting from the upscaled model with those from the classical Darcy equation (*i.e.*, assuming that the biomass is a solid phase) the contribution of the intracellular fluid phase was evidenced. This work sets the foundations for further studies dedicated to transport phenomena in this type of systems.

1. Introduction

Fungal cultures, filamentous and non-filamentous, are of interest in industry and research due to their essential role in many biotechnological processes. Some applications of fungal biomass are in wastewater treatment (Espinosa-Ortiz et al., 2016; Legorreta-Castañeda et al., 2020), environmental systems (Ángeles-Argáiz et al., 2020), enzymes and metabolites production for food, pharmaceutical and other industrial applications (Böl et al., 2020; El-Gendi et al., 2021).

In submerged agitated cultures, mycelia (*i.e.*, clusters of branching hyphae) grow intertwined and form hemispherical porous structures named (bio)pellets. Due to the complex geometrical configurations formed in these structures and the variation of hyphal density (or pellet porosity), different spatially homogeneous zones have been identified (Espinosa-Ortiz et al., 2016; Reyes et al., 2017; Li et al., 2020). The intricate hyphal topologies may hinder oxygen and nutrients transport within the inner part of the pellets, where hyphal density usually increases, leading to a decreasing metabolic activity when approaching the center of the pellets, even reaching cease of activity or lysis (Silva et al., 2001; Hille et al., 2005; Krull et al., 2010). The presence, topology, compactness and thickness of these regions depend upon the fungal species, mycelia age and culture conditions. The latter include culture medium composition, pH, inoculum size and characteristics, agitation and aeration rates, geometry and bioreactor scale, and, in the case of stirred tank bioreactors, the type of impeller used (therefore also

☆ **Funding information**: Programa de Apoyo a Proyectos de Investigación e Innovación Tecnológica, Universidad Nacional Autónoma de México (PAPIIT-UNAM, IN211422, IV201220).

* Corresponding author at: Departamento de Biología Molecular y Biotecnología, Instituto de Investigaciones Biomédicas, Universidad Nacional Autónoma de México, 04510, CDMX, Mexico.
E-mail address: maurotru@iibiomedicas.unam.mx (M.A. Trujillo-Roldán).

https://doi.org/10.1016/j.jtbi.2024.111853
Received 19 December 2023; Received in revised form 11 April 2024; Accepted 14 May 2024
Available online 18 May 2024

the power supplied per unit volume, shear stress and viscous energy dissipation with respect to circulation time, among others) (Shamlou et al., 1994; Hellendoorn et al., 1998; Cui et al., 1998a; Silva et al., 2001; Hille et al., 2005; Kelly et al., 2006; Duarte, 2009; Krull et al., 2010). Also, hyphae can be either septated or non-septated (coenocytic). In the former case, hyphae are divided by septa (permeable barriers), into compartments of roughly the same length (Mouriño-Pérez, 2013). Septa may play some key roles in momentum transport (Van Driel et al., 2008; Mouriño-Pérez, 2013). The first one is to increase rigidity of the hyphae by providing additional cellular wall. The second one is related to prevention, to a limited extent, of mechanical damage at growing-tip regions. The last one is to localize damage and cytoplasmic loss to a certain portion of the hyphae and thus protect the remaining compartments. Moreover, the structural complexity of the septal region is species-dependent. For example, Basidiomycota possess a specialized septa denominated *dolipores* that control mass and momentum transport between adjacent compartments (Sumbali et al., 2005). All these factors, which depend on the microstructure, significantly influence transport phenomena within agitated pellet cultures (Hille et al., 2005, 2009).

Mass and momentum transport at the scale of hyphae impact the microorganism metabolism, viability and product formation, which ultimately have repercussions in hyphal growth (Böl et al., 2020). It is therefore of prime importance to study the effects of transport phenomena inside fungal pellets of varying constitutive morphologies.

The culture of mycelium pellets is a hierarchical system with different levels of scale, regardless the type of vessel used (Nielsen and Krabben, 1995; Davidson, 2007). In a hierarchical system, transport phenomena at a given scale are determined by the corresponding phenomena at the inferior scale(s) (see, for instance, Sánchez-Vargas and Valdés-Parada, 2022). As shown in Fig. 1, the *hyphal scale* is the smallest one for this system and it is also denoted as the *microscale* in the following. Here, only the individual hyphae and the culture medium are distinguished. Moreover, the characteristic length may correspond to either the maximal hyphal thickness or to the maximal distance between hyphae, which are on the order of microns (Roberson et al., 2014; Vetchinkina et al., 2017). Next is the *pellet scale* (also denoted the *macroscale* in this work), where the characteristic length may be associated to the diameter of the fungal pellets, *i.e.*, on the order of hundreds of microns to millimeters (Pradella et al., 1990; Rossi et al., 2002, 2007). Finally, the largest scale corresponds to a portion of a flask or bioreactor, which is on the order of centimeters to meters. These two differ by the presence of bubbles in the bioreactor and incorporate different pellet sizes and disperse mycelium.

The mathematical models found in the literature can be grouped according to the scale hierarchy proposed above. At the scale of hyphae, probabilistic modeling has been used to describe their elongation and branching (Yang et al., 1992) and hyphal extension by vesicle incorporation to the tip wall (Bartnicki-Garcia et al., 1989), more recently expanded to a 3D model (Gierz and Bertnicki-Garcia, 2001) and including diffusive transport of vesicles (Tindemans et al., 2006). In the latter, vesicles are conceived as a chemical species for which mass transfer obeys Fick's law, and focus was laid on the extending tip of a hypha, neglecting convective transport with respect to diffusive transport on the basis of a sufficiently small Péclet number value. This assumption precludes the application of the model to regions of the hypha, within the same cell but far from the extending tip, in which cytoplasmic flow contribution to mass transport gains importance (Mogilner and Manhart, 2018). Deterministic modeling has been applied to describe the dynamics of the cytoskeleton (regarded as a viscoelastic fluid) and diffusive and advective (cytoskeleton-mediated) vesicle transport (Regalado and Sleeman, 1999). A different approach consists of the application of global species mass balances to model hyphal length extension due to turgidity and the concentration of vesicles or organelles based on their consumption or production rates and volume flow rates of the cytoplasm or the cytoskeleton (King, 2015).

At the scale of pellets, probabilistic modeling was used in the work of Meyerhoff and Bellgardt (1995), consisting of a model to represent the processes of spore germination, pellet fragmentation due to shear stress and the pre-culture and culture of up to 100 pellets. In the work by Lejeune and Baron (1997), the model was extended from spore germination to pellet formation using fractal geometry to represent the complex pellets structure. These works represent some of the few modeling approaches that connect the first two scales of the system depicted in Fig. 1: the hyphae and pellet scales. Other works deal with mass and substrate diffusive transport and reaction in pellets through postulated time- and space-dependent models (Davidson, 1998; Boswell, 2003). Some other analyses are based upon population models that render a time-dependent class distribution based on pellet sizes, as described by Tough et al. (1995) and Tough and Prosser (1996). These two works consider both pellets growth and death, as well as fragmentation due to shear stress in submerged cultures, with pellet fragments serving as germinal points for generating new pellets. At this scale level, diffusive mass transport models are frequently postulated in the form of average equations, where the effective diffusion coefficient needs to be experimentally quantified (Cui et al., 1998a; Silva et al., 2001; Celler et al., 2012; Schmideder et al., 2019, 2020). It has been shown that the assumption of diffusive-driven mass transport inside the fungal pellets is only valid in specific scenarios, such as in very compact structures (Hille et al., 2009). In less-dense pellets, substrates transport occurs through turbulent diffusion and convective flow (Schügerl et al., 1983; Wittler et al., 1986; Hille et al., 2005; Krull et al., 2010), thus highlighting the relevance of also studying fluid flow inside these structures.

Fluid flow at the microscale and macroscale have been scarcely studied in agitated pellet cultures, even though they provide valuable information about pellets mechanics and therefore represent the basis to study convective mass transport and relate it to the process productivity (Böl et al., 2020). Also, fluid flow analysis is required to study the effects of shear stress over pellet morphology by coupling the (total) mass and momentum balance equations. Moreover, momentum transport is fundamental in order to unveil the interconnection between growth, the mechanical forces applied, pellet shaving, species mass transport and vacuolization, some of the main factors that determine pellet structure and size during the culture (Paul et al., 1994; Shamlou et al., 1994; Cui et al., 1998b,a). This momentum multiscale analysis is typical in non-biological applications, such as catalytic inert pellets, fixed-bed reactors and other porous materials (Bear, 2018). Here Darcy or Darcy-like models are typically employed at the macroscale, which usually emerge as a result of an upscaling process of the governing equations at the microscale using methods such as volume averaging or homogenization (Kulkarni et al., 2008; Salejova et al., 2011; Das et al., 2018; Yang et al., 2023).

Upscaling techniques are adequate to study multiscale processes by systematically filtering the relevant information from the lower scale levels and allowing the final model predictions to be influenced by all the underlying scales. As a salient feature of upscaling, the resulting model is mathematically simpler than its microscale counterpart, facilitating its solution with less computational requirements. However, a drawback of upscaling approaches is that the analysis can only be performed in terms of average quantities. This implies that it is not possible to use the model to retrieve the detailed information at the lower scale levels. Also, accuracy of the upscaled model predictions strictly depends on the starting and upscaling assumptions taken in the following way. Firstly, the starting assumptions adopted at the microscale influence the pertinence with respect to naturally-occurring phenomena in the biological system. Given the complex nature of biological systems, approximations of the actual behavior are usually adopted. Secondly, upscaling assumptions should be carefully posed so

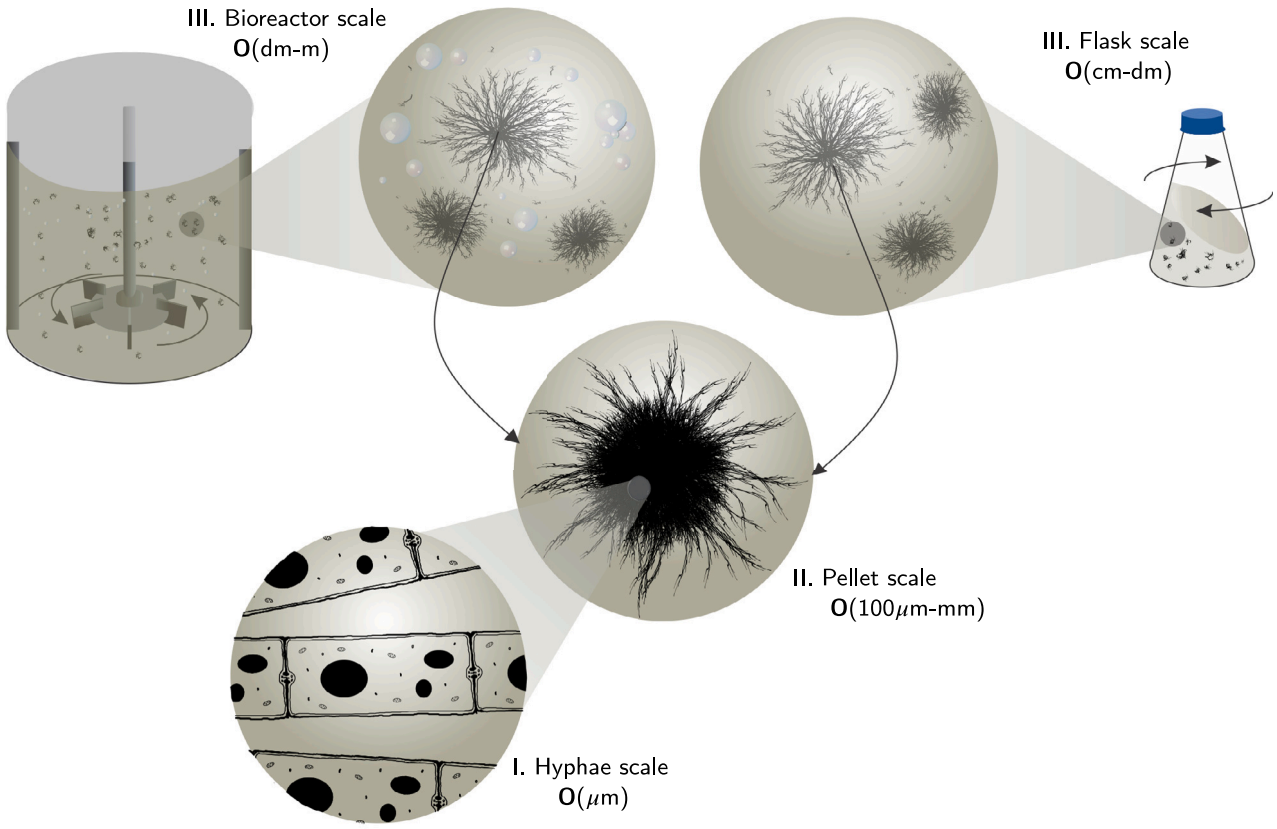

Fig. 1. Diagram representing a shake flask and an aerated stirred tank bioreactor as hierarchical systems for the culture of fungal pellets, with their corresponding characteristic lengths as order of magnitude estimates. At scale level I (microscale), the individual hyphae and surrounding culture medium that make up the fungal pellet are observed. Level II (macroscale) corresponds to a fungal pellet, conceived as a porous biological (hyphal) structure while the liquid phase corresponds to the culture medium that floods the pores. In level III, the flask or bioreactor scales are identified.

that the average model predictions are in agreement with the average of the model solution at the microscale.

The goal of the present study is to formulate and apply an upscaled fluid mechanics model, considering the essential microscale system characteristics of fungal pellets. This work is the starting point of several studies directed at modeling this complex multiscale system and will serve as a first step towards studying species mass transport. Derivations are made taking elements from the volume averaging method (Whitaker, 1999) and the adjoint homogenization approach (Bottaro, 2019), based on the works of Lasseux and Valdés-Parada (2022) and Sánchez-Vargas et al. (2023) for two-phase flow in porous materials. Results from the upscaling process are presented in Sections 3.2 and 3.3 for (total) mass and momentum transport, respectively. The mathematical model derived here has some generality as it is not formulated for a particular fungal species. However, to illustrate the use of the model, a case study using pellets of the ectomycorrhizal fungus *Laccaria trichodermophora* is considered. For this fungal species, a geometrical characterization of hyphae from shake flasks cultures, necessary for the model application, is presented in Section 3.4. A parametric analysis, along with the validation of the model via direct numerical simulations, are reported in Section 3.5. Finally, conclusions are drawn in Section 4.

2. Methodology

This section is divided in two parts. In the first one, the mathematical descriptions and tools for performing the upscaling of the total mass and momentum balances equations are provided. The second part corresponds to the experimental methodology used to quantify the required characteristics for application of the mathematical models on fungal pellets of *Laccaria trichodermophora*, chosen as a particular case study. Certainly, the model may be applied to any pellet-forming microorganism.

2.1. Mathematical definitions and tools

The derivation of the upscaled (macroscopic) mass and momentum balance equations can be made using a variety of techniques as reviewed by Battiato et al. (2019). In the present work, the upscaling process is performed taking elements from the volume averaging method (Whitaker, 1999), the adjoint homogenization approach (Bottaro, 2019) and Green's integral formulation. This approach requires accounting for the following elements: (1) the existence of an averaging domain, (2) the application of integral theorems, decomposition and series expansions and (3) the use of periodic unit cells. These three elements are explained in the following paragraphs.

2.1.1. Existence of an averaging domain

The application of an upscaling process is restricted to systems in which there is a separation of length scales between the microscale (ℓ) and the macroscale (L) (Battiato et al., 2019). As shown in Fig. 2, at the microscale, two phases are identified, namely, the extracellular fluid or culture medium, which is denoted as the γ phase, and the intracellular fluid (*i.e.*, the β phase). Both phases are separated by the fungal cell wall and membrane, which is modeled here as a dividing surface, for simplicity.

In this way, the characteristic length ℓ is associated to the maximum length between the width of the individual fungal cells (ℓ_β) or the distance between them (ℓ_γ). In the following, ℓ is assumed to be much smaller than the minimum length scale associated to the fungal

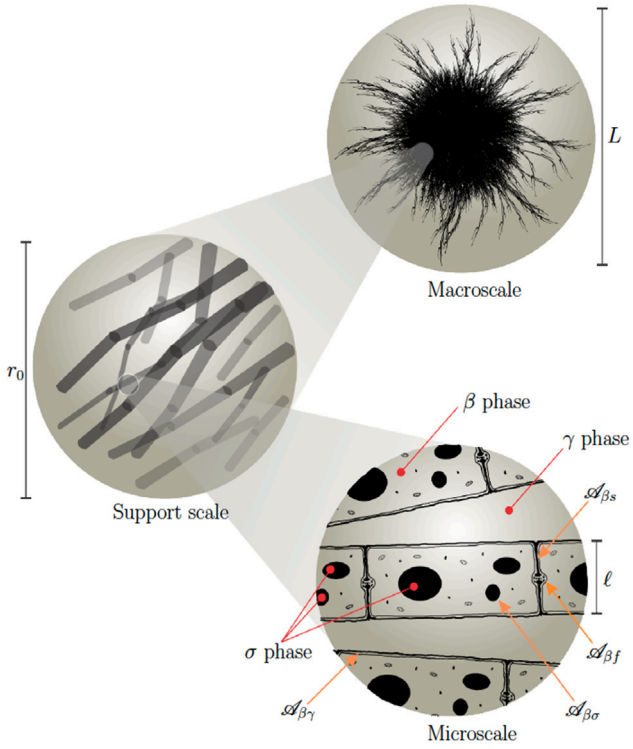

Fig. 2. Sketch of the scale hierarchy under study in the present work. The macroscale corresponds to a pellet and the microscale to a sample of hyphal compartments. The main phases and characteristic lengths are identified, as well as the support scale used during the upscaling procedure.

pellets (L). This motivates defining an intermediate scale between the microscale and the macroscale (*i.e.*, a *support* scale), of characteristic length r_0, at which upscaled models are applicable. Under this assumption, an averaging domain $\mathscr{V}$, of measure V, is defined, containing portions of all the phases that make up the system and being representative of the microscale configuration. In order to avoid losing important information from the microscale, r_0 must be much smaller than L. In systems in which the microscale geometry is regular (i.e., spatially periodic), ℓ and r_0 could be of the same order of magnitude. However, in biological systems that degree of homogeneity is rarely met. In most systems, a separation in two orders of magnitude is a constraint generally adopted to satisfy the representativeness of the domain of size r_0 (Whitaker, 1999). Regarding L, it must be larger (by two orders of magnitude) than r_0 to make upscaling pertinent. Nevertheless, it is worth remarking that this constraint on length scales separation may be overly severe and the upscaled models may still be applicable if there is only one order of magnitude of difference. In cases that do not comply with this last constraint, different approaches should be adopted, either by solving the microscale equations everywhere or using a different type of mathematical tool that allows application in non-regular geometries. Therefore, the characteristic length, r_0, of $\mathscr{V}$ is assumed to comply with the following constraint

$$\ell \ll r_0 \ll L. \tag{1}$$

It is desirable to experimentally verify this inequality prior to the application of the upscaled model so that the starting assumptions are met to assess its consistency with the model derivation.

In terms of the averaging domain, superficial and intrinsic averaging operators of a piece-wise continuous pore-scale quantity, ψ_α, defined anywhere within the α phase (in the following, the subscript α is used to represent either one of the fluid phases, *i.e.*, $\alpha = \beta, \gamma$), are respectively defined by

$$\langle \psi_\alpha \rangle_\alpha \big|_{\mathbf{x}_\alpha} = \frac{1}{V} \int_{\mathscr{V}_\alpha} \psi_\alpha \big|_{\mathbf{r}_\alpha} \, dV, \tag{2a}$$

$$\langle \psi_\alpha \rangle^\alpha \big|_{\mathbf{x}_\alpha} = \varepsilon_\alpha^{-1} \, \langle \psi_\alpha \rangle_\alpha \big|_{\mathbf{x}_\alpha} = \frac{1}{V_\alpha} \int_{\mathscr{V}_\alpha} \psi_\alpha \big|_{\mathbf{r}_\alpha} \, dV. \tag{2b}$$

Here, $\mathscr{V}_\alpha$ (of measure V_α) corresponds to the space occupied by the α phase in $\mathscr{V}$. Note that points in the α phase are located by the position vector $\mathbf{r}_\alpha$, with respect to a fixed coordinate system, while the resulting average is positioned at the barycenter of the α phase ($\mathbf{x}_\alpha = \langle \mathbf{r}_\alpha \rangle^\alpha$, as long as the α phase is incompressible). Moreover, the volume fraction of the α phase is defined as $\varepsilon_\alpha = V_\alpha / V$. When this macroscopic parameter exhibits negligible spatial variations within a given domain, such zone of the system can be classified as homogeneous at the support scale (Whitaker, 1999). Therefore, this parameter is used later on to determine the existence of homogeneous regions in the fungal pellets.

2.1.2. Integral theorems and series expansions

The averaging process requires using the general transport theorem (Bird et al., 2002) and the spatial averaging theorem (see for example, Howes and Whitaker, 1985). These theorems are used in order to exchange (temporal and spatial) differentiation and spatial integration.

Furthermore, a microscale quantity, ψ_α, can be expressed in terms of its intrinsic average and spatial deviations, $\tilde{\psi}_\alpha$, as defined by Gray (1975)

$$\psi_\alpha \big|_{\mathbf{r}_\alpha} = \langle \psi_\alpha \rangle^\alpha \big|_{\mathbf{r}_\alpha} + \tilde{\psi}_\alpha \big|_{\mathbf{r}_\alpha}. \tag{3}$$

Note that the average term is evaluated at the same point as ψ_α and not at the phase barycenter. To overcome this issue, a Taylor series expansion can be used as follows (see, for example, Lasseux and Valdés-Parada (2023))

$$\langle \psi_\alpha \rangle^\alpha \big|_{\mathbf{r}_\alpha} = \langle \psi_\alpha \rangle^\alpha \big|_{\mathbf{x}_\alpha} + \mathbf{z}_\alpha \cdot \nabla \langle \psi_\alpha \rangle^\alpha \big|_{\mathbf{x}_\alpha} + \frac{1}{2} \mathbf{z}_\alpha \mathbf{z}_\alpha : \nabla\nabla \langle \psi_\alpha \rangle^\alpha \big|_{\mathbf{x}_\alpha} + \dots. \tag{4}$$

Here, $\mathbf{z}_\alpha \equiv \mathbf{r}_\alpha - \mathbf{x}_\alpha$ is a position vector that locates the same point as $\mathbf{r}_\alpha$ but with respect to $\mathbf{x}_\alpha$. Substitution of the previous expression into Eq. (3) leads to

$$\psi_\alpha \big|_{\mathbf{r}_\alpha} = \tilde{\psi}_\alpha \big|_{\mathbf{r}_\alpha} + \langle \psi_\alpha \rangle^\alpha \big|_{\mathbf{x}_\alpha} + \mathbf{z}_\alpha \cdot \nabla \langle \psi_\alpha \rangle^\alpha \big|_{\mathbf{x}_\alpha} + \frac{1}{2} \mathbf{z}_\alpha \mathbf{z}_\alpha : \nabla\nabla \langle \psi_\alpha \rangle^\alpha \big|_{\mathbf{x}_\alpha} + \dots. \tag{5}$$

The above developments are used during the upscaling procedure while formulating the problem in a unit cell, as reported in the next paragraph.

2.1.3. Periodic unit cells

It is pertinent to mention that, for periodic realizations of the microstructure, the fluid velocity and deviations of other fields, like the pressure, can be assumed periodic over the averaging domain (Lasseux and Valdés-Parada, 2022). This leads to propose the solution of boundary-value problems not in the entire domain but in a periodic unit cell that captures the essential features of the microscale. The use of a periodic unit cell is a convenience more than a necessity. System-specific experimental measurements must be performed, leading to construction of geometries that may be incorporated in periodic unit cells to represent the microscale structure (Auriault et al., 2009). This also implies that the averaging domain has to have homogeneity, at least in its geometrical properties. In the paragraphs that follow, it is shown that, while working in a periodic unit cell, adjoint closure problems are defined in order to derive the macroscale model for momentum transport. This can be done by using Green's formula as reported in Appendix A of Sánchez-Vargas et al. (2022).

2.2. Experimental materials and methods

The model application requires the following information that can be obtained from experiments: (1) Measurement of the characteristic length scales ℓ and L in order to verify that $\ell \ll L$ (see (1)). (2) Quantification of the volume fraction of one of the fluid phases and determination of the existence of homogeneous regions inside the pellet. This step involves proposing values of r_0 that meet the inequality given in (1). (3) Information of the essential microscale geometrical features that should be incorporated in periodic unit cells. These experimental measurements are performed on fungal pellets of *L. trichodermophora* for illustration purposes.

2.2.1. Microorganism and culture

The CA15-F10 strain of *L. trichodermophora*, previously reported by Ángeles-Argáiz et al. (2020), was used. Biotin Folic Acid (BFA) culture medium was employed for plate culture, as well as liquid pre-inoculum and inoculum preparation, in the following composition: dextrose, 10 g L^{-1}; peptone from gelatin, 2 g L^{-1}; yeast extract, 0.2 g L^{-1}; potassium phosphate dibasic (KH_2PO_4), 0.5 g L^{-1}; magnesium sulphate, ($MgSO_4 \cdot 7H_2O$) 0.5 g L^{-1}; calcium chloride ($CaCl_2$), 0.1 g L^{-1}; zinc sulphate ($ZnSO_4$), 1 mg L^{-1}; manganese sulphate ($MnSO_4$), 5 mg L^{-1}; thiamine HCl, 50 μg L^{-1}; biotin, 1 μg L^{-1}; folic acid, 100 μg L^{-1}; inositol, 5 μg L^{-1}. The pH was set to 5.50 ± 0.05 with the addition of 0.5 M HCl, and 10 g L^{-1} of bacteriological agar was added for solid medium preparation (Ángeles-Argáiz et al., 2020). All reagents were purchased from Merck-Sigma-Aldrich (USA).

For pre-inoculum preparation, three samples of approximately 9 mm^2 were cut from the periphery of 15-days-old colonies growing in BFA plates and used to inoculate a 250 mL Erlenmeyer baffled flask with 50 mL of BFA liquid medium (Gamboa-Suasnavart et al., 2011). The latter was grown for 10 days (until the exponential phase) under a controlled temperature of 25 ± 2 °C in an orbital shaker (C25 New Brunswick Scientific, USA), with an orbital diameter of 2.54 cm, at 100 rpm. From this flask, 1 mL of culture medium containing hyphae was used to inoculate a 250 mL baffled flask with 50 mL fresh BFA liquid medium (inoculum flask). The inoculum was incubated at 25 ± 2 °C and agitation at 100 rpm for 10 days was carried out.

From the inoculum, 1 mL of medium containing hyphae was taken, 2% v/v, and added to 250 mL Erlenmeyer baffled flasks with 50 mL of defined culture medium with a carbon:nitrogen ratio of 16:1 and pH of 5.5 ± 0.1. The composition of the defined medium is that of BFA, replacing the complex nutrients (peptone from gelatin and yeast extract) with 0.554 g L^{-1} urea and 20 g L^{-1} MES buffer ($C_6H_{13}NO_4S \cdot xH_2O$). These baffled flasks were incubated at 25 ± 2 °C and agitated at 100 rpm in the same orbital shaker (C25 New Brunswick Scientific, USA).

2.2.2. Pellets and clumps imaging and processing

From baffled flask cultures, clumps and pellets were taken with a pipette and visualized on light microscopy. A Nikon A1R+ STORM confocal microscope was used in bright field, performing mosaic acquisitions in the median plane of each pellet. The images were processed with Fiji software (ImageJ2 version 2.9.0/1.53t) (Rueden et al., 2017).

2.2.3. Volume fraction determination in pellets

Four baffled flasks were inoculated and cultured as described in Section 2.2.1. A flask was taken on days 7, 14 and 21 (inter-spaced days during *L. trichodermophora* growth curve) and three samples of pellets were randomly selected from each flask. Samples were fixed and glucose-infiltrated following Vasquez-Martínez et al. (2023). Briefly, they were fixed with a 4% paraformaldehyde solution for 24 h and subsequently rinsed 4 times with phosphate-buffered saline (PBS 0.1 M, pH 7.4, with: 0.026 g L^{-1} $NaH_2PO_4 \cdot H_2O$, 0.127 g L^{-1} Na_2HPO_4 and 0.085 g L^{-1} NaCl) buffer solution. Afterwards, the pellets were incubated at 4 °C for 1 h in a 10% sucrose solution and then for 1 h at 4 °C in a 20% sucrose solution. Finally, they were incubated for 24 h in a 30% sucrose solution at 4 °C. Individually, the pellets were placed in molds, embedded in Tissue Freezing Medium (Leica Biosystems) and freezed at −20 °C for 20 min. Frozen pellets were stored at −20 °C until sectioned. A Leica CM1520 cryostat operated at −18 °C was used for the sectioning and 13 μm thickness sections were obtained. They were placed on gelatin-adhesive slides, allowed to dry, and stained with toluidine blue.

Three cuts at different depths of each pellet were selected and serial photographs along their diameter (as depicted in Fig. 3(a)) were taken with a Nikon Optiphot 2 microscope in bright field with a 20x objective. Later, the images were processed in the Fiji software (ImageJ2 version 2.9.0/1.53t) (Rueden et al., 2017). Each image was converted to 16-bit, the *mean* method was used to adjust the threshold, and each photograph was divided by overlapping a grid with a random origin. The space occupied by the hyphae was quantified, starting at the center of the vertical axis, in square regions (averaging surfaces) of different sizes, namely 100, 200, 300, 400, 500, 600, 700, 800 and 900 μm in side length. With these measurements, the extracellular volume fraction was calculated at different positions with respect to the pellet diameter (x axis) and with different sizes of the averaging surface.

Finally, the extracellular volume fraction corresponding to each averaging surface from each pellet section was quantified. This was done according to the scheme illustrated in Fig. 3(b). For each averaging surface within each section, located by its centroid, x, a unique value of the volume fraction was computed. This value results from averaging the phase indicator (taking the value 1 in the phase of interest and 0 elsewhere) in the x and y directions, thus compacting the structural information over the corresponding 2D region into a point value. A final computation of the mean and standard deviation of all the values was also performed.

2.2.4. Hyphae length and width measurements inside the pellets

From baffled flasks of 6–8 days of growth, young pellets and clumps (of approximately 3 mm in diameter, including both the core and hyphal projections of the pellet) were taken and stained with FM4-64 (N-(3-triethyl-ammoniumpropyl)-4-(6-(4-(diethylamino) phenyl) hexatrienyl) pyridinium dibromide, Molecular Probes, Thermo Sci. USA) at a concentration of 10 μM and an incubation time of 2 min. Stained cellular structures were observed on a LSM800 inverted laser scanning confocal microscope with an incubation chamber maintained at 25 °C, using a Plan-Apochromat 63x/1.4 oil immersion objective and a 488 nm laser line. Transmitted light images were obtained with an Electronically Switchable Illumination and Detection (ESID) module, and images of both channels were recorded simultaneously. Tile scans of Z-stacks acquired at 0.3 μm intervals (1-2 μm in depth) were obtained for the complete diameter of each pellet. The hyphal length and width were quantified with the Fiji software at every section of the pellets.

2.2.5. Dolipore visualization and measurements

Four baffled flasks were inoculated and cultured as described in Section 2.2.1. A flask was taken on days 7, 14, and 21, and three pellets were randomly selected. Samples were treated with a methodology based on that reported by Antonio-Rubio et al. (2015) as follows. Pellets were fixed with a 4% paraformalin + 3% glutaraldehyde solution for 24 h and washed twice with PBS. A 1% osmium tetroxide post-fixation was performed for 1 h and then washed with distilled water. Two successive rinses, with increasing concentrations of ethanol, were used for the dehydration of the samples. These concentrations were: 60%, 70%, 80%, 90%, 96% and 100%. Afterwards, 2-propylene oxide washes were done. Subsequently, the impregnation of the resin in the samples was carried out gradually in the following order: epon:propylene oxide (1:2) for 1 h, epon:propylene oxide (1:1) for 24 h, epon:propylene oxide (2:1) for 24 h, epon pure for 24 h. The inclusion was carried out in silicone molds at 60 °C in an oven, for at least 24 h. The pellets were stored until cut at room temperature.

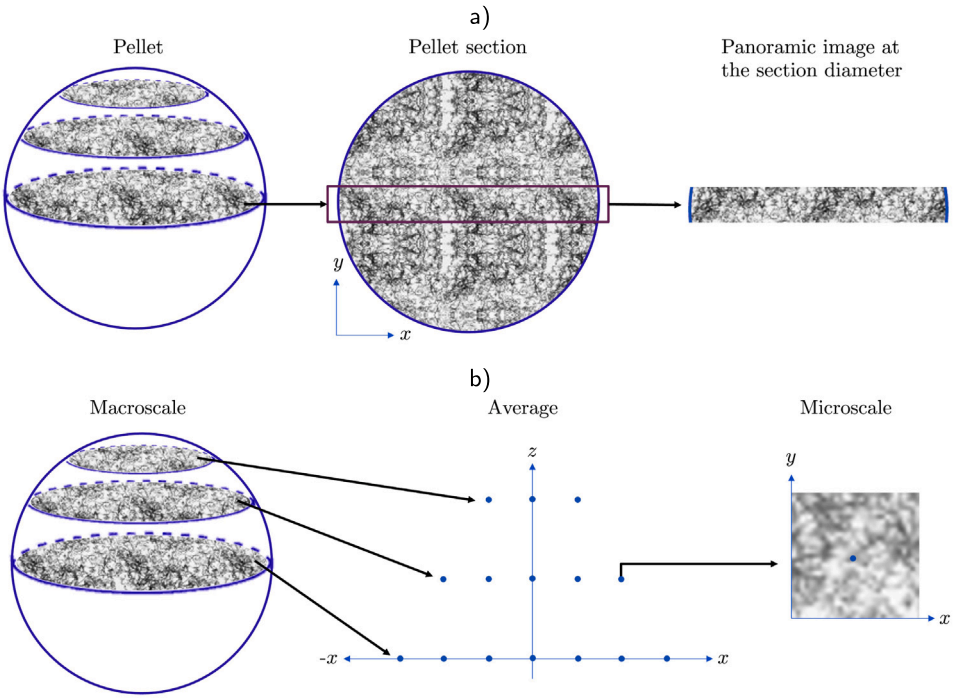

Fig. 3. (a) Scheme of the procedure for experimental determination of the volume fraction of pellets. The procedure consists of making sections at different positions in the z direction and subsequently taking photographs along the section diameter. (b) Scheme of the averaging process at every position of the panoramic images. The process consists of compacting the information within averaging surfaces of the pellets section into a value that represents the volume fraction that is located at the geometric center, x, of the averaging surface.

The pellets were sectioned at different positions along their diameter with a Leica Ultracut UCT ultramicrotome and a diamond blade. The sections were made with a thickness of 70 nm and placed in copper grids. The grids were double contrasted with uranyl acetate and lead citrate. To summarize, each grid was impregnated with 2.5% uranyl acetate for 10 min in a closed petri dish, protected from light. After abundant rinsing with Milli-Q water and drying, grids were impregnated with 0.3% alkaline lead citrate in a Petri dish, protected from light. Finally, grids were rinsed and let dry. Observations were performed in a LIBRA 120 Carl Zeiss transmission electron microscope for the quantification of the dolipore width.

3. Results and discussion

The formulation and implementation of the flow model in fungal pellets is reported. For this purpose, the first step is the statement of the microscale governing equations for fungal cultures that serve as a basis for upscaling of the total mass and momentum transport models presented next. The following step is the experimental characterization of *L. trichidermophora* that is detailed before finally presenting the upscaled model predictions in a periodic unit cell constructed with the experimental data. The intention here is to illustrate the whole methodology that may be employed to model any other pellet-forming microorganism.

3.1. Governing equations at the microscale

Here, the governing equations for total mass and momentum transport at the microscale are presented along with the corresponding boundary conditions. This implies adopting a set of starting assumptions, which are kept at minimum in order for the resulting upscaled model to be applicable over a wide range of biological systems.

Focusing on (total) mass transport, assuming that both the intracellular and extracellular phases are incompressible (*i.e.*, the fluid density in each phase is constant both in space and time), the following expression is applicable at the microscale (Bird et al., 2002)

$$\nabla \cdot \mathbf{v}_\alpha = 0, \quad \text{in the } \alpha \text{ phase}, \tag{6a}$$

where $\mathbf{v}_\alpha$ is the fluid velocity in the α phase ($\alpha = \beta, \gamma$).

In both the extra- and intracellular phases, momentum transport is assumed to be stationary, *i.e.*, time acceleration is neglected with respect to viscous effects. In addition, inertial effects are known to be relevant at least in the extracellular phase, as the Reynolds number inside the pellets has been estimated to be in the range between 7 and 300, for *Aspergillus niger*, depending on pellet size and power input during the culture (Hille et al., 2005). Thus, for the sake of generality, inertial contributions are included in both phases. Also, gravity is considered as the only volume force in the system and its effects are included in both phases. Furthermore, a generalized Newtonian model for momentum transport is adopted in both phases. In the extracellular phase, this allows accounting for the influence of the concentration of salts and organic compounds from the culture medium and the accumulation of compounds produced by the microorganism to the extracellular medium during culture, as well as loose hyphae contributing to rheology at upper scale levels (see, for example, Bliatsiou et al. (2020) for pellet culture of filamentous fungi). In addition, the intracellular fluid is assumed to include the cytosol, organelles, vesicles, proteins and polymer networks. Therefore, it can be regarded as a pseudo-liquid phase. These components contribute to the rheology in this phase as reported by Mogilner and Manhart (2018). Furthermore, the cytoplasm of eukaryotic cells is known to have viscoelastic characteristics due to its content of cytoskeletal polymers, proteins and small organelles (Stamenović, 2008; Ahmed et al., 2018; Mathieu and Manneville, 2019). Consequently, the viscous stress tensor in both fluid phases ($\boldsymbol{\tau}_\alpha$, $\alpha = \beta, \gamma$) is given by $\boldsymbol{\tau}_\alpha = \mu(\Gamma_\alpha)(\nabla \mathbf{v}_\alpha + \nabla \mathbf{v}_\alpha^T)$, with $\mu(\Gamma_\alpha)$ being the apparent viscosity, which depends on the strain rate modulus, $\Gamma_\alpha = \sqrt{\frac{1}{2}\left(\nabla \mathbf{v}_\alpha + \nabla \mathbf{v}_\alpha^T\right) : \left(\nabla \mathbf{v}_\alpha + \nabla \mathbf{v}_\alpha^T\right)}$.

On the basis of the above considerations, following Bird et al. (2002), the equations that describe momentum transport at the microscale for the extracellular and intracellular fluid phases are ($\alpha = \beta, \gamma$)

$$\rho_\alpha \mathbf{v}_\alpha \cdot \nabla \mathbf{v}_\alpha = \rho_\alpha \mathbf{g} + \nabla \cdot \mathbf{T}_{p_\alpha} \quad \text{in the } \alpha \text{ phase,} \tag{6b}$$

where the total stress tensor is defined as $\mathbf{T}_{p_\alpha} = -\mathbf{I}p_\alpha + \boldsymbol{\tau}_\alpha$. Moreover, ρ_α and p_α are, respectively, the density and pressure of the α phase and $\mathbf{g}$ is the gravity acceleration vector.

As mentioned in the previous section, the cell wall and membrane are modeled as a dividing surface, which is denoted as $\mathscr{A}_{\beta\gamma}$ (see Fig. 2). This is justified since the characteristic width of the cell wall and membrane is much smaller than the characteristic size of the cells (*i.e.*, ℓ_β). At this boundary the most significant resistance to momentum transport occur. This is attributed to the structure of the cell wall, which is usually made of an arrangement of chitin and β-glucans that are coupled to a diverse set of polymers and glycosylated proteins, conferring the cell wall resistant but flexible characteristics. These properties allow the cell wall to comply with its biological function, acting as a protective boundary but also allowing growth, as well as nutrients and vesicles transport (Gow and Lenardon, 2022). Consequently, the stress jump condition can be written in the following form (Slattery et al., 2006)

$$\mathbf{n}_{\beta\gamma} \cdot \left(\mathbf{T}_{p_\beta} - \mathbf{T}_{p_\gamma} \right) = \boldsymbol{\zeta} \quad \text{at } \mathscr{A}_{\beta\gamma}. \tag{6c}$$

Here, $\mathbf{n}_{\beta\gamma}$ is the unit normal vector at $\mathscr{A}_{\beta\gamma}$, directed from the β to the γ phase. In addition, the vector $\boldsymbol{\zeta}$ represents the mechanical resistance of the cell wall and membrane, $\mathscr{A}_{\beta\gamma}$.

At this same boundary, continuity of the velocity fields in both phases is assumed to apply (see, for instance, Slattery et al., 2006). This is,

$$\mathbf{v}_\beta = \mathbf{v}_\gamma \quad \text{at } \mathscr{A}_{\beta\gamma}. \tag{6d}$$

This condition can be justified on the basis of the following. Firstly, although transport of chemical species takes place at the cell wall and membrane, it is assumed that this process does not change significantly the densities in both the intracellular and extracellular phases. This justifies continuity of the normal component of the velocity vectors in each phase, equal to the normal component of the speed of displacement of the cell wall and membrane, $\mathbf{w}$. This is,

$$\mathbf{n}_{\beta\gamma} \cdot \mathbf{v}_\beta = \mathbf{n}_{\beta\gamma} \cdot \mathbf{v}_\gamma = \mathbf{n}_{\beta\gamma} \cdot \mathbf{w}, \quad \text{at } \mathscr{A}_{\beta\gamma}. \tag{6e}$$

Secondly, slip effects between the extra- and intracellular fluids at $\mathscr{A}_{\beta\gamma}$ are disregarded, which justifies assuming continuity of the tangential components of the velocity vectors.

In this work, momentum transport within the organelles is not considered. This is because in agitated pellet cultures, when moving from the extracellular medium to the organelles, there are many boundaries, including cell wall, cell membrane and organelle membranes, which are assumed to provoke a marked decrease in the amount of momentum experienced inside the organelles. In this way, momentum transport within the organelles is neglected with respect to momentum transport in the extra- and intracellular phases. In the following, large organelles (denoted as the σ phase and with a characteristic length > 1 μm, see Fig. 2) are assumed to behave as rigid and immobile solid inclusions that are impervious to momentum transport. This also implies that a no-slip boundary condition applies at the β-σ interface ($\mathscr{A}_{\beta\sigma}$).

The focus of this model relies on non-septate hyphae for the sake of simplicity. The cell–cell boundary ($\mathscr{A}_{\beta\beta'}$) can have different morphologies depending on the fungal species under study. At these segments of the hypha, for some fungal species, the septum might completely separate adjacent compartments, while, for other species, septal pores are located at the mid-section of the septum. Moreover, these pores can be either open or occluded, as they play a role in regulation of mass and momentum transport along the hypha. If the septal pore is completely open or only partially occluded, momentum transport will take place between hyphal compartments (adjacent segments of the hypha that are separated by a septum). This means that, under these conditions, the surface $\mathscr{A}_{\beta\beta'}$ can be divided into a septated portion where $\mathbf{v}_\beta = \mathbf{0}$ ($\mathscr{A}_{\beta s}$) and another one available for flow ($\mathscr{A}_{\beta f}$). In the latter, the velocity field is assumed periodic in the single spatial direction perpendicular to $\mathscr{A}_{\beta f}$. The above can be expressed as follows

$$\mathbf{v}_\beta = \mathbf{0}, \quad \text{at } \mathscr{A}_{\beta\sigma}, \mathscr{A}_{\beta s}, \tag{6f}$$

$$\mathbf{v}_\beta(\mathbf{r}) = \mathbf{v}_\beta(\mathbf{r} + \mathbf{l}_f), \quad \text{at } \mathscr{A}_{\beta f}. \tag{6g}$$

Here $\mathbf{r}$ and $\mathbf{l}_f$ respectively represent a position vector and the periodic lattice vector. Notice that no momentum transport takes place in an occluded pore, when present. This is because of the presence of a complex group of membranes, wall material and the dense proteinaceous plug at this surface, which limits momentum transport between adjacent compartments. Consequently, in this case the boundary condition at $\mathscr{A}_{\beta f}$ reduces to the one given in (6f). Nevertheless, the boundary conditions given in Eqs. (6f) and (6g) are general and are kept as such in the developments that follow.

3.2. Upscaling mass transport

This section focuses on upscaling the total mass transport equations in both the intracellular and extracellular phases, using Eq. (6a) as a starting point. The resulting macroscale balance equation has been already derived in previous works dedicated to multi-phase flow in porous media systems (see for example Whitaker, 1986; Auriault, 1986) and the derivation is not repeated here. It shall be recalled that it results from applying the superficial averaging operator (Eq. (2a)) to Eq. (6a), and using the general and spatial averaging theorems, taking into account the interfacial boundary conditions. The resulting expression can be written in the following form

$$\frac{d\varepsilon_\alpha}{dt} + \nabla \cdot \langle \mathbf{v}_\alpha \rangle_\alpha = 0. \tag{7}$$

To apply the above equation, the system has to comply with the starting assumptions. Nevertheless, Eq. (7) does not require assuming periodicity of the system geometry at the microscale.

The first term in Eq. (7) accounts for the temporal variations of the volume fractions of each fluid phase and it can be associated to biomass growth (when ε_β increases) or mycelium lysis (when ε_β decreases) inside the pellet. These observations can be used in future works, where total mass balance is coupled with species transport equations to model cellular growth as reported by Wood and Whitaker (1999). The temporal dependence at the macroscale arises from the possible transient character of the cell wall and membrane, implicitly making the momentum problem at the microscopic scale time-dependent. This is true even if temporal acceleration is neglected with respect to viscous effects in the momentum transport equations, as considered above.

It should be noted that, in steady state, the first term on the left-hand side of Eq. (7) is zero. Furthermore, the same result is obtained if the system geometry is spatially periodic so that the microscale fluid velocity in each phase is also periodic. In this way, $\langle \mathbf{v}_\alpha \rangle_\alpha$ is spatially-invariant and Eq. (7) reduces to $d\varepsilon_\alpha/dt = 0$. Therefore, under any of these two circumstances the macroscopic mass balance equations reduce to

$$\nabla \cdot \langle \mathbf{v}_\alpha \rangle_\alpha = 0, \quad \mathscr{V} \text{ periodic or } \mathscr{A}_{\beta\gamma} \text{ stationary.} \tag{8}$$

3.3. Upscaling momentum transport

Recently, Sánchez-Vargas et al. (2023) derived an upscaled model for steady non-Newtonian inertial two-phase flow in homogeneous porous media. Although the physical system is strictly not the same here, the governing equations and boundary conditions at the microscale are very similar. In fact, the difference lies in the incorporation of the cell–cell boundary conditions given in Eqs. (6f) and (6g) and differences in the boundary condition expressed in Eq. (6c). For this

reason, only the essential steps leading to the upscaled momentum balance equations are recalled below and the reader is referred to the work by Sánchez-Vargas et al. (2023) (see also (Lasseux and Valdés-Parada, 2022)) for a detailed description of the whole procedure.

It is convenient to adopt the periodic unit cell assumption at the beginning of the derivations (Lasseux and Valdés-Parada, 2022). It must be emphasized that this assumption does not represent a limitation as it only exerts an influence at the closure level (microscale), with a vanishing effect at the macroscale. Furthermore, upscaled models that employ volume averaging (or other upscaling techniques that imply the periodicity assumption, such as homogenization (Auriault et al., 2009)), have been successfully used in practice, even in non-periodic systems (see, for example Nolen et al. (2008)). The procedure shown below consists in deriving a formal average solution of the flow problem by defining adjoint closure problems and relating them to the momentum transport equations using a Green's function formalism. Therefore, it is convenient (albeit not mandatory) to consider periodic unit cells to reduce the solution domain of the adjoint closure problems.

In a periodic unit cell, both the velocity and pressure spatial deviations can be assumed to be periodic. In this regard, Gray's decomposition in the form given in Eq. (5) is applied to the terms containing the pressure in the microscale model (Eqs. (6)). It is worth recalling that, at the unit cell level, the macroscopic pressure gradient can be reasonably assumed to be constant. Under these conditions, the momentum transport problem in a periodic unit cell can be written as $(\alpha = \beta, \gamma)$

$$\nabla \cdot \mathbf{v}_\alpha = 0, \quad \text{in } \mathscr{V}_\alpha, \tag{9a}$$

$$\rho_\alpha \mathbf{v}_\alpha \cdot \nabla \mathbf{v}_\alpha = -\nabla \langle p_\alpha \rangle^\alpha + \rho_\alpha \mathbf{g} + \nabla \cdot \mathbf{T}_{\tilde{p}_\alpha} \quad \text{in } \mathscr{V}_\alpha, \tag{9b}$$

$$\mathbf{n}_{\beta\gamma} \cdot \left(\mathbf{T}_{\tilde{p}_\beta} - \mathbf{T}_{\tilde{p}_\gamma} \right) = \mathbf{n}_{\beta\gamma} \left(\langle p_\beta \rangle^\beta \Big|_{\mathbf{x}_\beta} - \langle p_\gamma \rangle^\gamma \Big|_{\mathbf{x}_\gamma} \right) + \mathbf{n}_{\beta\gamma} \mathbf{z}_{\beta\gamma} \cdot \nabla \langle p_\beta \rangle^\beta \Big|_{\mathbf{x}_\beta} - \mathbf{n}_{\beta\gamma} \mathbf{z}_{\gamma\beta} \cdot \nabla \langle p_\gamma \rangle^\gamma \Big|_{\mathbf{x}_\gamma} + \boldsymbol{\zeta} \quad \text{at } \mathscr{A}_{\beta\gamma}, \tag{9c}$$

$$\mathbf{v}_\gamma = \mathbf{v}_\beta, \quad \text{at } \mathscr{A}_{\beta\gamma}, \tag{9d}$$

$$\mathbf{v}_\beta = \mathbf{0}, \quad \text{at } \mathscr{A}_{\beta\sigma} \text{ and } \mathscr{A}_{\beta s}, \tag{9e}$$

$$\mathbf{v}_\beta(\mathbf{r}) = \mathbf{v}_\beta(\mathbf{r} + \mathbf{l}_f), \quad \text{at } \mathscr{A}_{\beta f}, \tag{9f}$$

$$\psi(\mathbf{r} + \mathbf{l}_i) = \psi(\mathbf{r}), \quad i = 1, 2, 3; \ \psi = \mathbf{v}_\alpha, \tilde{p}_\alpha, \tag{9g}$$

$$\langle \tilde{p}_\alpha \rangle^\alpha = 0, \tag{9h}$$

with

$$\mathbf{T}_{\tilde{p}_\alpha} = -\mathbf{I}\tilde{p}_\alpha + \mu(\Gamma_\alpha) \left(\nabla \mathbf{v}_\alpha + \nabla \mathbf{v}_\alpha^T \right). \tag{9i}$$

Eq. (9g) represents the periodicity condition in the three directions, with $\mathbf{l}_i$ being the unit cell lattice vectors ($\sum_i \mathbf{l}_i = \mathbf{l}_f$). In addition, Eq. (9h) is an integral constraint for the pressure deviations, which is necessary to have a well-posed problem. In addition, note that in Eq. (9c) the Taylor series expansion given in Eq. (4) was used.

At this point, it is convenient to emphasize that the resulting average pressures contained in Eqs. (9) arise from different sources. In the extracellular phase, the pressure is the consequence of applied agitation, whereas in the intracellular phase, the macroscopic pressure is related to cytoskeleton-associated (Charras et al., 2008) and osmotic pressure generated (Keren et al., 2009) forces, these last two capable of acquiring similar orders in magnitude (Mogilner and Manhart, 2018). The latter, is caused by the higher ion concentration in the intracellular fluid with respect to the extracellular medium. Furthermore, as shown in Appendix B of the work by Lasseux and Valdés-Parada (2022), the macroscopic pressure gradients in both fluid phases can be safely assumed to be the same.

In order to advance towards the derivation of macroscale balance equations, adjoint closure problems are proposed and reported in Appendix A.1 (see Bottaro (2019) for details on how adjoint problems are constructed for upscaling).

The flow problem defined in Eqs. (9) can then be related to the adjoint closure problems by means of Green's formula as detailed by Sánchez-Vargas et al. (2023). This leads to the following macroscopic momentum balance equations in each phase $(\alpha, \kappa = \beta, \gamma)$

$$\langle \mathbf{v}_\alpha \rangle_\alpha = -\frac{\mathbf{H}_{\alpha\alpha}}{\mu_{ref\alpha}} \cdot \left(\nabla \langle p_\alpha \rangle^\alpha - \rho_\alpha \mathbf{g} \right) - \frac{\mathbf{H}_{\alpha\kappa}}{\mu_{ref\kappa}} \cdot \left(\nabla \langle p_\kappa \rangle^\kappa - \rho_\kappa \mathbf{g} \right) + \frac{1}{\mu_{ref\alpha} V} \int_{\mathscr{A}_{\beta\gamma}} \boldsymbol{\zeta} \cdot \mathbf{D}_{\alpha\alpha} \, dA + \frac{\rho_\gamma - \rho_\beta}{\mu_{ref\alpha} V} \int_{\mathscr{A}_{\beta\gamma}} \mathbf{n}_{\beta\gamma} \cdot \mathbf{ww} \cdot \mathbf{D}_{\alpha\alpha} \, dA. \tag{10}$$

Here, $\mathbf{H}_{\alpha\alpha}$ and $\mathbf{H}_{\alpha\kappa}$ $(\alpha \neq \kappa)$ are, respectively, the dominant and coupling apparent permeability tensors in the α phase, which are defined as

$$\mathbf{H}_{\alpha\alpha} = \langle \mathbf{D}_{\alpha\alpha} \rangle_\alpha^T, \quad \mathbf{H}_{\alpha\kappa} = \frac{\mu_{ref\kappa}}{\mu_{ref\alpha}} \langle \mathbf{D}_{\kappa\alpha} \rangle_\kappa^T. \tag{11}$$

In the above equations, $\mathbf{D}_{\alpha\alpha}$ and $\mathbf{D}_{\kappa\alpha}$ are closure variables that solve problems (A.1) and (A.2).

Eqs. (10) describe the average velocity of the fluid in the α phase (either the intracellular or extracellular fluid), in terms of four contributions: two bulk (Darcy-like) terms and two interfacial terms. The first (dominant Darcy-like) term represents the contribution to the flux, resulting from the macroscopic forcing applied in the phase under consideration, whereas the second (coupling Darcy-like) term describes, through viscous coupling, the contribution of the macroscopic pressure gradient in the adjacent phase. The last two terms in Eqs. (10) are the interfacial contributions to the movement of the fluids, one accounts for mechanical resistance effects, while the other one is produced by inertia at $\mathscr{A}_{\beta\gamma}$.

To conclude, it is pertinent to make three remarks about the macroscale model derived in the previous sections and its application. First, it is important to recall the underlying requirements that include satisfying the separation of length scales, as stated in inequality (1), which needs to be confirmed through experimental quantification of the constitutive elements of the system, *i.e.*, the hyphae and pellet characteristic lengths in the present work. Also, as described in Section 3.1, the system must be composed of two incompressible fluids (extra- and intracellular fluids) separated by a delimiting element (in the present biological application, a cell wall and membrane) and a phase behaving as an immobile solid (in this case, the organelles) only in contact with one phase (the wetting phase, in the present case, the intracellular fluid). No restriction is imposed concerning the fluids rheology, as the model allows them to acquire a generalized Newtonian nature. Moreover, the intracellular fluid must be divided, either partially or completely, into compartments. It must be noted that this last configuration, if not encountered, requires the correction of the boundary conditions stated above in the microscale model, as well as in the closure problems with, nevertheless, the same upscaling methodology.

Second, it is important to summarize the experimental information required from a particular biological system in order to apply the model. This includes the existence of representative regions inside the pellet, where the system topology should remain spatially homogeneous on average. This can be assessed by verifying that the volume fractions of the phases remain constant. Also, and for the purpose of constructing the representative periodic unit cell, the length and width of the hyphal compartments and the determination of the presence and size of the septal pores is needed. Note that the system geometry is not required to be spatially periodic in order to apply the macroscale models. Furthermore, if periodicity cannot be reasonably assumed, as it may be the case in systems where there is no clear separation of length scales (for example in clumps or very small pellets), then the closure problems solution can still be applied, albeit in domains larger than a single unit cell. For convenience, the model can be solved in a

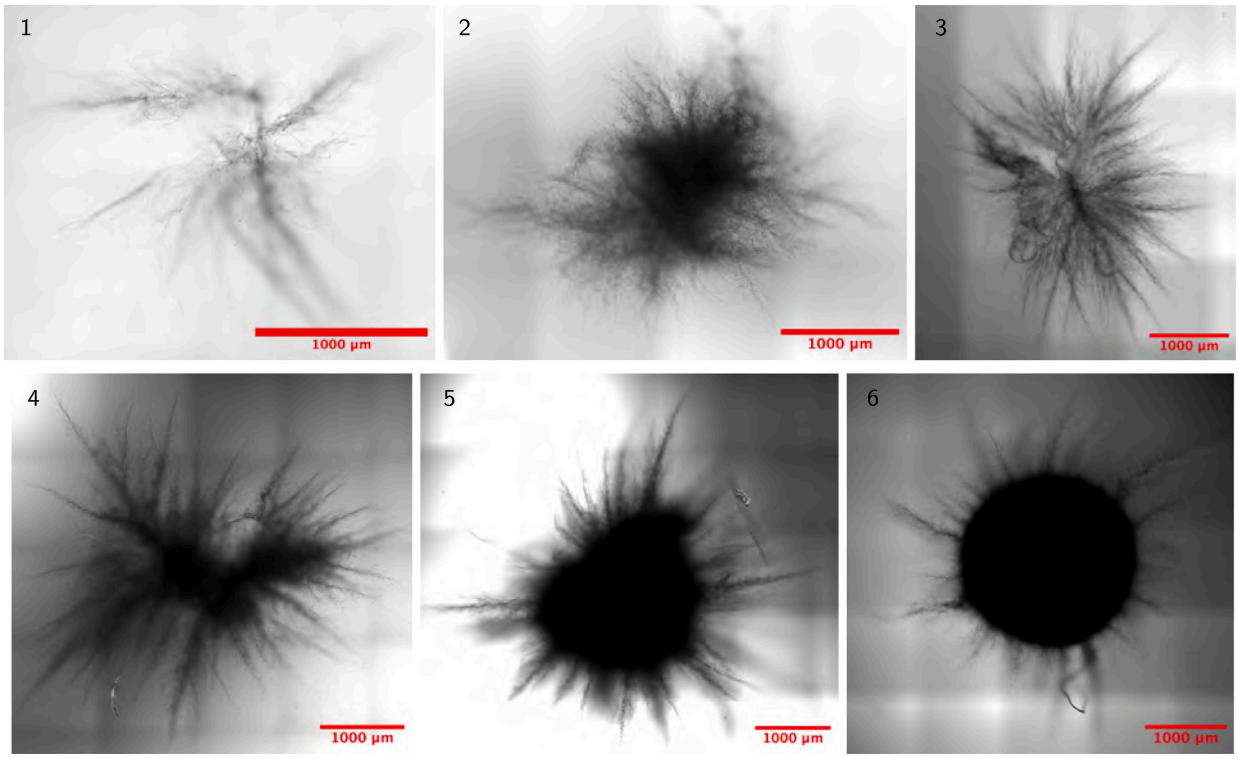

Fig. 4. Bright-field micrography of clumps and pellets of *L. trichodermophora*, illustrating, in six different stages, the formation of consolidated pellets (hemispherical structures possessing a dense core and loose hyphal projections) from hyphal clumps (agglomeration of hyphae starting at their initial growing stage) during culture in agitated baffled flasks. The biomass is classified according to geometrical characteristics and size: young clumps (stages 1–2), mature clumps (stages 3–4), young pellets (stage 5) and consolidated pellets (stage 6). This process takes place constantly during the culture, which gives place to clumps and pellets of different sizes at all stages of the culture.

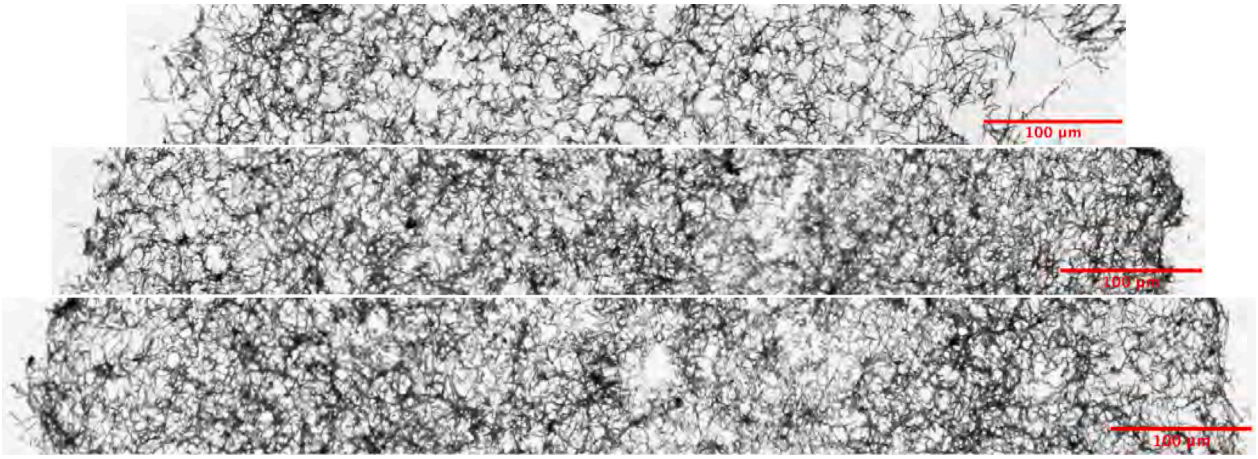

Fig. 5. Sections of the core of a 7 days-old fungal pellet of *L. trichodermophora*, of 448 μm in radius, at successive z positions measured from the center of the pellet: 0 μm (bottom), 95 μm (middle) and 181 μm (top).

dimensionless form, thus reducing the number of degrees of freedom. The parameters needed are the Reynolds number, the fluids viscosity ratio and rheological parameters of the fluid phases (precise definitions are given later on in Section 3.5).

Third, as a result from the solution of the upscaled model, the predictions that this model provides are in terms of the average velocity of each fluid phase. Moreover, since the macroscale momentum model explicitly expresses all the contributions to the average velocity, each of them can be separately evaluated. This includes the determination of the intrinsic or apparent permeabilities of the pellets, depending on the presence of inertia, and the interfacial contributions to the average velocity.

3.4. Characterization of Laccaria trichodermophora

This section accounts for the experimental information required for the upscaled models application in geometries representative of *L. trichodermophora* pellets. It must be noted that, given the generality of the derived model, any other pellet-forming microorganism could have been used instead for the characterization and further evaluation of the model.

An increase in size and hyphal density is observed by bright field confocal microscopy at the different stages of pellet formation (Fig. 4). Based on their geometrical characteristics and size, the following nomenclature is adopted in the remainder of the article. Stages 1 and

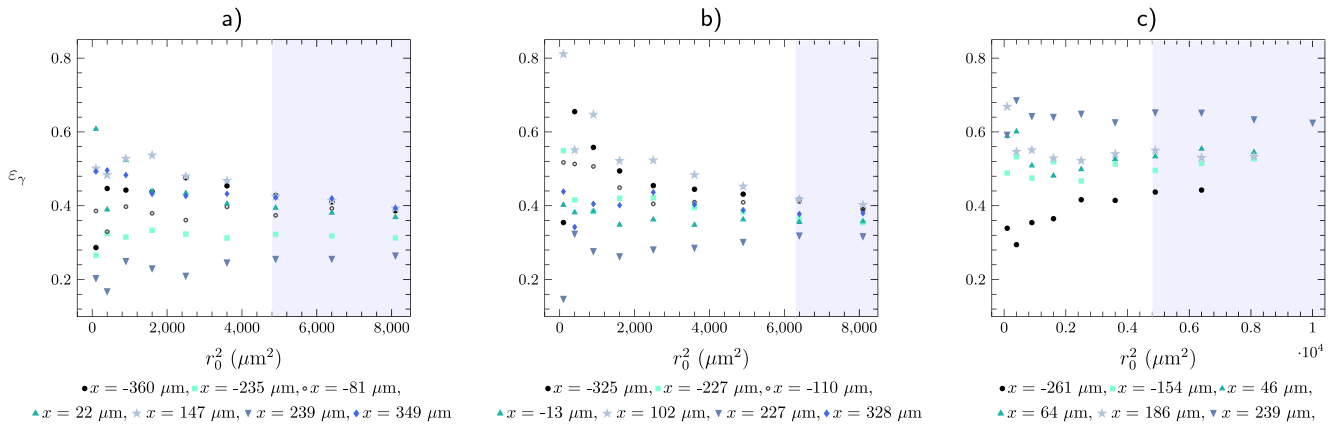

Fig. 6. Dependence of the volume fraction of the extracellular phase, ε_γ, with the area of the averaging surface for 7 days-old pellet sections (see Fig. 5) at different positions in z and x. r_0^2 indicates the area of the averaging surface. Each series represents a different position with respect to the center of the x axis of the pellet. (a) z = 0 μm, (b) z = 95 μm, (c) z = 181 μm. The shaded blue area represents the interval of r_0 corresponding to a representative size of the averaging surface.

2 are denoted as *young clumps*, stages 3 and 4 correspond to *mature clumps*, stage 5 comprises *young pellets* and stage 6 corresponds to *consolidated pellets*.

3.4.1. Identification of homogeneous regions

Pellets of *L. trichodermophora* are hemispherical structures with a dense hyphal core and hyphal projections (Fig. 4, stages 5 and 6). In order to determine the presence of homogeneous regions inside the pellets, 13 μm-thick sections were obtained from randomly selected stage-6 pellets, following the sampling procedure depicted in Fig. 3. Three sections per pellet (taken at different z positions) were analyzed, providing panoramic images of the core of a 7 days-old pellet (Fig. 5). The same type of analysis was performed on 14 and 21 days-old pellets (figures S1 and S2, respectively). It is important to notice that the hyphal projections do not exhibit spatially homogeneous regions, thus precluding the use of the model derived in this work in this zone of the pellets. Conversely, the pellets core appears to comply with this assumption. To confirm this observation, spatial properties were evaluated on square regions of different sizes, which are referred to as averaging surfaces, at different positions on the x axis of the three sections obtained for each pellet.

For an averaging surface to be representative of the microscale, macroscopic properties (such as the volume fraction or permeability) must exhibit negligible variations as the averaging surface size changes. In the system under consideration, the volume fraction of the extracellular fluid phase, ε_γ, was experimentally quantified for this purpose. The results corresponding to a 7 days-old pellet are shown in Fig. 6(a)–(c) for sections at different positions in the z-direction. In all these figures, ε_γ takes values from about 0.15 to 0.8, oscillating for smaller areas of the averaging surface and stabilizing above a certain threshold of averaging surface size, which depends upon the specific section. For the section at 0 μm in the z position and 896 μm in diameter (Fig. 5, bottom), ε_γ stabilizes at a value of the area of the averaging surface of 4900 μm^2. The same is true for the section at 181 μm in the z position (Fig. 5, top). However, for the 865 μm section, located at 95 μm on the z axis, stability is reached at 6400 μm^2 (see Fig. 5, middle). For all these sections, the value of ε_γ remains roughly constant until the last value of r_0^2 that was considered, *i.e.*, 8100 μm^2 (Fig. 6(a) and (b)) and 10,000 μm^2 (Fig. 6(c)). This means that the appropriate value of r_0 is within the range of 70 and 100 μm. Representativeness may be even better achieved with r_0 larger than 100 μm. However, in the present experiment, the limit was the width of the panoramic image and the random positioning of the grid used for quantification. The results presented for a 7 days-old pellet of *L. trichodermophora* indicate the existence of homogeneous regions, regardless the positions under consideration, inside the structure. This meets the upscaling method assumption previously stated. Similar results were obtained for the 14 and 21 days-old pellets (figures S3 and S4, respectively).

The extracellular volume fraction, ε_γ, varies along the pellet diameter in the range from about 0.25 to 0.65 for 7, 14 and 21 days-old pellets (Fig. 7). The average values of ε_γ in each pellet core and the corresponding standard deviation confirm some degree of homogeneity between the pellets of different sizes and culture times and can be estimated to be 0.405 ± 0.091, 0.369 ± 0.082 and 0.352 ± 0.096 (with no significant differences among them), respectively for the 7, 14 and 21 days-old pellets. Given the evident dispersion of ε_γ seen in Fig. 7, there are two possible approximations to use the upscaled model in this type of pellets. The first and more rigorous one is to solve the model in each homogeneous regions, which implies a solution for every value of volume fraction experimentally determined. This could be followed by a second averaging of the model predictions for a determined region, section or the whole pellet core. The second approximation consist in solving the upscaled model only for the average volume fraction of the pellet core, providing in this way a unique average velocity. For any of the above scenarios, it is still interesting to evaluate the effect of the volume fraction on the prediction of the average velocity in each phase. Therefore, values of ε_γ in the range from 0.3 to 0.65 will be used in Section 3.5 for the numerical simulations to evaluate the validity of the upscaled model in a fungal pellet. It must be noted that the presence of homogeneous regions was only assessed in pellets that were on stages 5 and 6, because they are compliant with the separation of length scales. As a final note, the fact of the volume fraction of the pellets core is time-independent (as the average ε_γ from the 7, 14 and 21 days-old pellets are statistically the same) is in agreement with the quasi-steady assumption for momentum transport (see Section 3.1).

3.4.2. Geometrical features at the microscale

Now that the existence of homogeneous regions inside the pellet has been confirmed and the value of r_0 has been established, the hyphae, which are the basic element of the microstructure, must be characterized in order to construct a periodic unit cell in which the closure problems derived in Section 3.1 are to be solved. Young pellets and clumps (stages 2–5 of Fig. 4) of 6–8 days old were used to determine characteristics of the hyphae in three regions of the structure, namely the periphery, middle and center. These regions were identified by subdividing the panoramic images into five equal parts. In this way, the diametrically-opposed parts correspond to the periphery regions, while the two adjacent ones are referred to the middle regions and the remaining part is the center. With this procedure, it was assumed that these younger structures had similar hyphal geometries as pellets in stages 5 and 6.

A typical configuration of hyphae inside a mature clump is shown in Fig. 8, where stained cell membranes are visualized along the radius

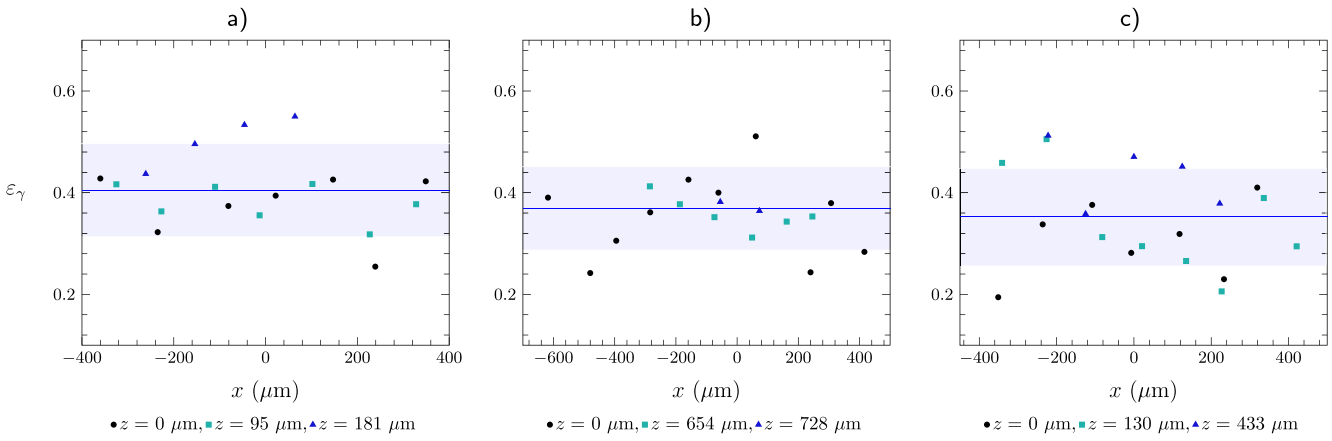

Fig. 7. Spatial dependence of the volume fraction of the extracellular phase, ε_γ, in the z and x directions for (a) 7 days-old pellet, (b) 14 days-old pellet and (c) 21 days-old pellet. (a) • $z = 0$ µm (corresponding to a 896 µm section), ■ $z = 95$ µm (corresponding to a 865 µm section), ▲ $z = 181$ µm (corresponding to a 704 µm section). (b) • $z = 0$ µm (corresponding to a 1500 µm section), ■ $z = 654$ µm (corresponding to a 743 µm section), ▲ $z = 728$ µm (corresponding to a 512 µm section). (c) • $z = 0$ µm (corresponding to a 1070 µm section), ■ $z = 130$ µm (corresponding to a 1040 µm section), ▲ $z = 433$ µm (corresponding to a 631 µm section). The blue line represents the average value of ε_γ in each pellet, obtained by averaging ε_γ of each individual homogeneous region in the pellet. The shaded blue region represents the interval of twice the standard deviation computed from the data, centered on the average value of ε_γ.

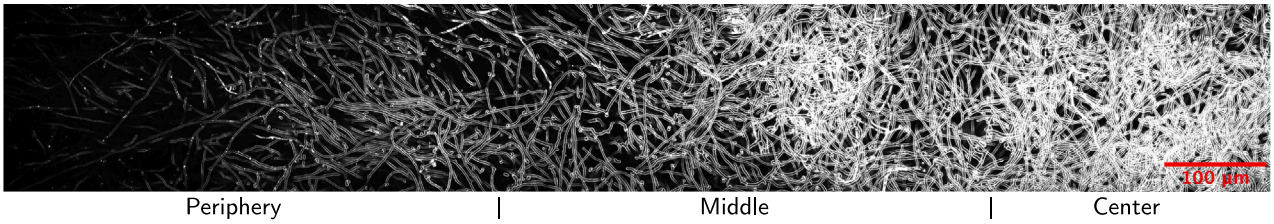

Fig. 8. Typical configuration of hyphae inside a mature clump of *L. trichodermophora* of 6 days of culture. The panoramic image corresponds to the left half of the pellet. Fluorescence signal corresponds to membranes stained with FM4-64. The vertical marks at the bottom of the image indicate the approximate limits of the periphery, middle and center regions.

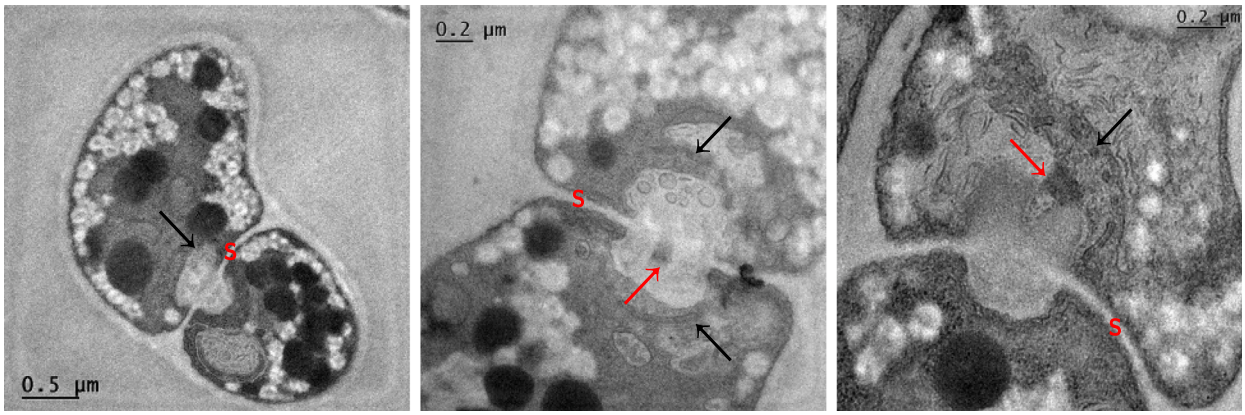

Fig. 9. Transmission electron micrographs of dolipore structures taken at the core of a fungal pellet of *L. trichodermophora* of 7 days of culture. **S**: septum, black arrow: parenthesome, red arrow: dolipore plug.

of a 6 days-old mycelial structure. Note that only three of the five parts in which the panoramic image was segmented are shown, as this image corresponds to only half of the pellet diameter. In this figure, a much denser network of hyphae is observed in the center, while the periphery is less populated, in accordance with Fig. 4.

Through image analysis, the hyphae width, length (determined as the distance between adjacent septa) and branching frequency were measured in the three different established regions (Table 1). With these results, it is evident that even if hyphal compartments have the same width among the defined regions, the length significantly increases towards the periphery. Note that the cell length is approximately two orders of magnitude larger than its width. This relationship is relevant and will be used in Section 3.5 for the construction of the periodic unit cell representative of the microstructure. In addition, it is important to remark that even though branching (*i.e.*, the increase in the amount of branches measured for a single compartment) takes place in the center and middle sections, the frequency is less than two. Furthermore, the vast majority of the young pellets and clumps volume corresponds to non-branched hyphae. For these reasons, branching is not considered in the unit cell design.

As mentioned, the fulfillment of the separation of length scales between the microscale and the macroscale needs to be verified. For this, the characteristic lengths to be taken into account correspond to those of the hyphae width (ℓ) and homogeneous regions of the

Table 1
Geometrical characteristics of hyphae through different sections of three young pellets and clumps of *L. trichodermophora* cultures grown in baffled shake flasks.

Concept	Measurement
Structure diameter[d]	3.33 ± 0.60 mm
Hyphae width[e]	1.79 ± 0.31 μm
Hyphae length (periphery)	155.44 ± 40.99 μm[a]
Hyphae length (middle)	103.75 ± 17.86 μm[b]
Hyphae length (center)	76.23 ± 16.99 μm[c]
Branches per hyphal compartment (periphery)	0
Branches per hyphal compartment (middle)	0–1
Branches per hyphal compartment (center)	1–2

[a,b,c] Indicate significant difference ($p < 0.0002$) among hyphal lengths belonging to different positions of the pellets and clumps. ANOVA, using Tukey post hoc test.
[d] Including the pellet core and hyphal projections.
[e] No difference was observed in cell width among the established regions, therefore only one measurement is reported. In the center of the pellets very few irregular hyphae can measure up to 2.6 μm thick, these were not considered in the analysis. This measurement was confirmed via transmission electron microscopy.

pellet (r_0). As reported in the above sections, $r_0 > 70$–90 μm, while $\ell = 1.79$ μm, suggesting a contrast of almost two orders of magnitude. In addition, the characteristic length of the pellets, L, is on the order of 10^3 μm. Therefore, the constraint given in inequality (1) is met. At this point it is pertinent to ponder about the applicability of the model to other types and sizes of pellets. To address this query, it is suggested that the following configurations could certainly be studied with the model derived in this work: Small (since 100 μm in characteristic length or two orders of magnitude above the width of the hyphae) dense or loose pellets with regular inner structures. Large (with no upper limit in characteristic length) dense or loose pellets that do not possess a void domain at the center (due to cell lysis or any other factor), in any case the model could only be applied to the remaining homogeneous regions bordering the void center and far from their borders.

The dolipore-parenthesome complex in Agaricomycotina plays a role in the selective transport of material between hyphal compartments, while allowing cytoplasmic continuity, when the channel remains unplugged (Patton and Marchant, 1978) and in general to cellular homeostasis (Van Driel et al., 2008; Van Peer et al., 2009). In this case, the factors determining the magnitude of the space for fluid flow are both the diameter of the dolipore channel (*i.e.*, the free space for fluid flow, located in the dolipore structure and communicating hyphal compartments, subject to obstruction by a septal plug) and the diameter of the parenthesome holes, which behave as a sieve, preventing large organelles to block the flow through the dolipore (Van Driel, 2007). In Fig. 9 three different locations of inter-compartmental division structures of *L. trichodermophora* are reported. The images show the septum, the dolipore and the associated perforate parenthesome. It must be noted that some of the dolipore structures appear to be associated with multivesicular or membrane bodies. This follows previous reports, where parenthesomes, which arise either from the endoplasmic reticulum or share a common ancestor with it (Van Driel, 2007; Van Peer et al., 2010), have been found to play a role in dolipore plugging by either producing or storing pore-plug material (Van Driel, 2007). For *L. trichodermophora*, the average length for fluid flow through the dolipore (pore channel) was evaluated to be 98.9 ± 7.6 nm (roughly 6% of the hypha width), while the pores of the parenthesome have an average diameter of 76.6 ± 7.0 nm. This feature is recalled during the construction of the periodic unit cell.

In some cases, a plug of proteins (septal plug), which is placed in the dolipore channel, can be found depending on the needs of the hypha and has evolved to protect intracellular content during stress or hyphal damage (Van Driel et al., 2008). The presence of either an open or closed dolipore channel is dynamic and depends upon many factors including culture conditions such as carbon source availability, temperature, osmotic pressure or presence of toxic agents (Van Peer et al., 2009). In Fig. 9, it can be noted that the middle and right pictures exhibit a septal plug, seen as an electron-dense occluding material (Van Driel et al., 2008), blocking protoplasmic streaming and therefore momentum transport. As noted by Van Peer et al. (2009), the probability of a plugged dolipore channel increases from the tip to the more distal compartments of hyphae. In the case of *L. trichodermophora*, the possibility of dolipores open to flow is considered, thus suggesting two different configurations of periodic unit cells to be used for numerical experiments in the following section.

All the measurements reported in this section are consistent (*i.e.*, of the same order of magnitude) with those reported in the literature for other Agaricomycetes or Agaricales. For instance, Roberson et al. (2014) reported images of the Agaricomycete *Auriscalpium vulgare*, where cells width and spacing for flow between hyphal compartments were measured to be of about 6 μm and 50 nm, respectively. Raudaskoski (2019) reported hyphal compartments length of around 150 μm for the Agarical *Schizophyllum commune*. Vetchinkina et al. (2017) studied the Agaricomycetes *Ganoderma lucidum*, *Grifola frondosa* and the Agarical *Lentinula edodes* and described cells of width between 3 and 4 μm, while the space for flow through the dolipore of *G. lucidum* and *G. frondosa* were quantified to be about 40 nm and 60 nm, respectively. Venneman et al. (2020) observed dolipore channels in nine different *Serendipita* species (Agarycomicetes) and quantified them in the range from 95 ± 31 nm to 128 ± 17 nm. Patton and Marchant (1978) analyzed the dolipore structure of 12 Agaricomycetes, among which there were four Agaricales, and reported parenthesome pore diameters mostly between 51 ± 8 nm and 143 ± 8 nm when excluding Aphilloporales. These observations are of relevance, as they suggest that the same architecture of periodic unit cell could be used to study many other species of Agaricomycetes.

3.5. Macroscopic model predictions

Before proceeding to the solution of the upscaled model, it is important to recall all the steps required for its application in any other (bio)pellet aside from the strain used here. First, the biological system to analyze must satisfy the starting assumption stated in Section 3.1. Second, experimental information about the biological system needs to be acquired, as described in Section 2.2, and the upscaling method assumptions must be confirmed. Third, the solution requires the construction of a 3D geometry, representative of the system configuration, in which the closure problems solution can be carried out in order to predict the macroscopic transport coefficients.

Employing the experimental data, two periodic unit cell configurations were constructed for every volume fraction value (see Fig. 10). All the unit cells keep the same proportions of the cellular compartments, which consist in curved cylinders with ellipsoids and spheres inside representing large organelles (>1 μm in characteristic length), impervious to momentum transport. It is assumed that these shapes are able to represent most of the organelles as a first approximation, since information in the literature is scarce for *L. trichodermophora* or other Basidiomycota. This choice could certainly be improved to include more complex geometries in future works. To generate unit cells with different volume fractions of the extracellular fluid, ε_γ, the quadrangular prism representing this phase was increased or decreased in size (by increasing the width of the quadrangular base of the prism), but the cellular volume (including the intracellular fluid and organelles) remained unaltered. The volume fraction of the extracellular fluid was varied from 0.30 to 0.65, while the organelle volume fraction (with respect to the intracellular content) was arbitrarily fixed to 0.39. The mycelium curvature was given by a cosine function, whose amplitude corresponds to the maximum possible fitting inside the γ phase domain. Consequently, the amplitude increased with ε_γ.

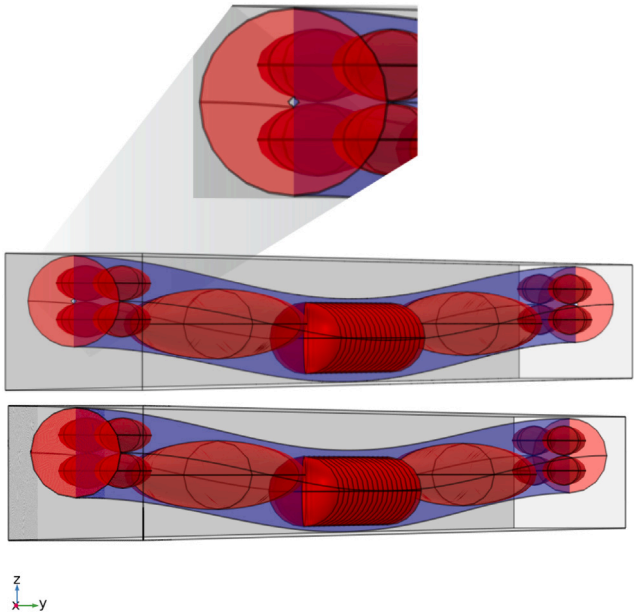

Fig. 10. Scheme of a representative unit cell used for the closure problems solutions. The figures correspond to a single mycelial compartment with an open (middle) or closed (bottom) dolipore channel. The difference resides in the presence of a pore in the center of the face on both ends of the cell length (top image). Proportions between the length and width of the mycelial compartment, as well as the dolipore channel width, correspond to those from Section 3.4.2 with an arbitrary curvature. In this particular case, $\varepsilon_\gamma = 0.65$ and the curvature is given by the function $0.00225\cos(2\pi s)$, where s is the position in the x direction. Periodicity was imposed in every direction of the unit cells.

With the unit cell at hand, the microscopic mass and momentum balance equations are solved (this is referred to as the direct numerical simulation, DNS, in the following) assuming that body forces can be lumped into the macroscopic pressure gradient (yielding a modified macroscopic pressure gradient). Moreover, flow in both phases is assumed to result from a horizontal macroscopic pressure gradient forcing (along the x axis). Note that this forcing could also be applied in other directions, depending on the biological system. This force can be understood as the result of the stress exerted during agitation by the walls of the flask onto the bulk fluid which further transfer the forcing to the pellet. In the present case, it is taken as

$$\nabla\langle p_\alpha\rangle^\alpha = \frac{\partial\langle p_\alpha\rangle^\alpha}{\partial x}\mathbf{e}_x = -h\mathbf{e}_x. \tag{12}$$

The next step towards the solution of the model is to impose any additional required simplification with the purpose of adapting the general model derived here to particular scenarios and, incidentally, facilitating the computation of the solution. The possible assumptions that can be reasonably imposed depend upon the specific biological system under concern. In the rest of this section, the analysis is restricted to situations in which the cell wall and membrane only oppose mechanical resistances in the direction orthogonal to $\mathscr{A}_{\beta\gamma}$. This is, $\boldsymbol{\zeta} = \zeta\mathbf{n}$, where ζ is a constant scalar in Eq. (6c). This means that the tangential mechanical contribution of the cell wall and membrane is assumed negligible with respect to its normal and constant counterpart. This assumption also allows simplifying the upscaled model. This is because, after application of the divergence theorem and taking into account the solenoidal nature of the closure variables (see Eqs. (A.1a) and (A.2a)), the third term on the right-hand side of Eq. (10) vanishes.

To reduce the number of degrees of freedom of the upscaled models, the dimensionless definitions reported in Appendix B of Sánchez-Vargas et al. (2023) are adopted and are recalled here as follows (the superscript * denotes dimensionless quantities)

$$\mathbf{r}^* = \frac{\mathbf{r}}{\ell_c}, \quad \mathbf{v}_\alpha^* = \frac{\mathbf{v}_\alpha t_{ref}}{\ell_c}, \quad p_\alpha^* = \frac{p_\alpha t_{ref}}{\mu_{ref\alpha}},$$

$$H^* = H\ell_c, \quad \mu^* = \frac{\mu_{ref\beta}}{\mu_{ref\gamma}}, \quad Re_\alpha = \frac{\rho_\alpha \ell_c^2}{\mu_{ref\alpha} t_{ref}}. \tag{13}$$

Here, ℓ_c is the length of the unit cell in the x direction, $t_{ref} = \frac{\mu_{ref\gamma}}{h\ell_c}$ is a reference time and h is the value of the macroscopic pressure gradient in the x direction (see Eq. (12)). Moreover, Re_α is the Reynolds number in the α phase. In addition, the macroscopic forcing defined in Eq. (12) takes the following dimensionless form

$$\nabla^*\langle p_\alpha^*\rangle^\alpha = -\mu_{ref\gamma}/\mu_{ref\alpha}\mathbf{e}_x. \tag{14}$$

Using the above definitions and the assumptions stated in Section 3.3 and in previous paragraphs, the macroscopic velocities in the α phase ($\alpha = \beta$ or γ) can be written in their dimensionless form as

$$\langle \mathbf{v}_\alpha^*\rangle_\alpha = \boldsymbol{\xi}_{\alpha\alpha}^* + \boldsymbol{\xi}_{\alpha\kappa}^* + \boldsymbol{\omega}_\alpha^*, \quad \alpha \neq \kappa, \tag{15}$$

where the following nomenclature is used

$$\boldsymbol{\xi}_{\alpha\alpha}^* = \frac{\mu_{ref\gamma}}{\mu_{ref\alpha}}\mathbf{H}_{\alpha\alpha}^* \cdot \mathbf{e}_x, \tag{16a}$$

$$\boldsymbol{\xi}_{\alpha\kappa}^* = \frac{\mu_{ref\gamma}}{\mu_{ref\kappa}}\mathbf{H}_{\alpha\kappa}^* \cdot \mathbf{e}_x, \tag{16b}$$

$$\boldsymbol{\omega}_\alpha^* = \frac{\mu_{ref\gamma}\left(Re_\gamma - Re_\beta\mu^*\right)}{\mu_{ref\alpha}V^*}\int_{\mathscr{A}_{\beta\gamma}} \mathbf{n}_{\beta\gamma}\cdot\mathbf{w}^*\mathbf{w}^*\cdot\mathbf{D}_{\alpha\alpha}^*\, dA^*. \tag{16c}$$

Here, $\boldsymbol{\xi}_{\alpha\alpha}^*$ and $\boldsymbol{\xi}_{\alpha\kappa}^*$ are defined as the dominant and coupling Darcy-like terms, respectively. Also, $\boldsymbol{\omega}_\alpha^*$ stands for the interfacial term accounting for inertial effects.

It must be noted that the dimensionless microscale flow problem and closure problems differ from those in Sánchez-Vargas et al. (2023) only in the boundary conditions, where an additional boundary between mycelial compartments has been incorporated in the present work. For the sake of brevity, these problems are not written here in their dimensionless form as they can be straightforwardly inferred from the above reference.

For the numerical simulations, the culture medium (γ phase) is considered to be Newtonian while the intracellular fluid (β phase) viscosity is supposed to obey the Carreau model given in the form

$$\mu(\Gamma_\beta) = \mu_\infty + (\mu_0 - \mu_\infty)\left[1 + (\lambda\Gamma_\beta)^2\right]^{(n-1)/2}. \tag{17}$$

Here, μ_∞ and μ_0 ($= \mu_{ref\beta}$) are the infinite and zero shear-rate viscosities, λ is the relaxation time, n the power-law index and $\Gamma_\beta = \sqrt{(\nabla\mathbf{v} + \nabla\mathbf{v}^T) : (\nabla\mathbf{v} + \nabla\mathbf{v}^T)/2}$ is the strain-rate modulus. Following the works of Airiau and Bottaro (2020) and Sánchez-Vargas et al. (2022), it is assumed that $\mu_\infty = 0$. Moreover, taking into account the definitions in Eq. (13) and considering that $\mu_{ref\beta} = \mu_0$, the Carreau model can be written in its dimensionless form as

$$\frac{\mu(\Gamma_\beta)}{\mu_{ref\beta}} = \left[1 + (\lambda^*\Gamma_\beta^*)^2\right]^{(n-1)/2}. \tag{18}$$

In the above equation $\Gamma_\beta^* = \Gamma_\beta t_{ref}$ and $\lambda^* = \lambda/t_{ref}$. For the numerical simulations carried out in this work, n was set to 1.2, while λ^* was fixed to 5, for the intracellular (β) phase. This combination of parameters implies that the intracellular phase behaves as a shear-thickening fluid (*i.e.,* the apparent viscosity increases with the shear rate) (Amoo and Fagbenle, 2020). Fluids that exhibit this type of behavior are concentrated suspensions (Amoo and Fagbenle, 2020), which resemble the conditions found inside fungal cells.

To solve the closure problems, as well as to perform DNS (for validation), the finite-element software Comsol Multiphysics 6.1 was employed, using a direct MUMPS solver. A mesh refinement analysis was performed to guarantee that the results are independent of the mesh size. Once DNS was performed, the average velocities over the unit cell were computed in order to further compare them to their predictions form the macroscopic model for validation of the latter. It may be argued that DNS would require the numerical solution of the microscale flow model in an array of unit cells. However, since the fluid

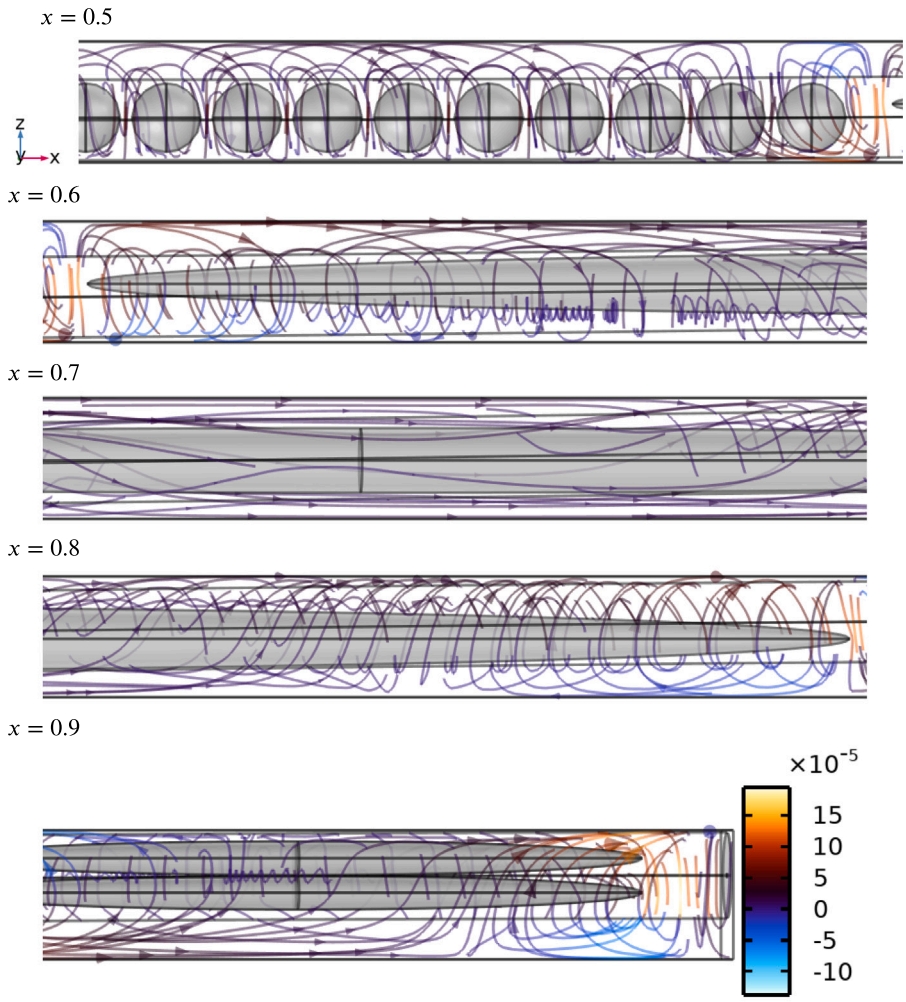

Fig. 11. Streamlines of the dimensionless intracellular and extracellular flow fields resulting from the solution of the microscopic flow problem (DNS) in a unit cell of a mycelial compartment with an open dolipore channel. Results are reported for five consecutive positions of 0.1 dimensionless length along the x axis, from top to bottom the left corner corresponds to: $x = 0.5$, $x = 0.6$, $x = 0.7$, $x = 0.8$, $x = 0.9$. Other parameters are $\varepsilon_\gamma = 0.65$, $\mu^* = \mu_{ref\beta}/\mu_{ref\gamma} = 5$, $Re_\gamma = 1$, $Re_\beta = 0.1$, $n = 1.2$ and $\lambda^* = 5$. Gray objects represent large organelles (≥1 μm in characteristic length).

velocity in both phases, as well as the geometry, are assumed periodic, it is sufficient to perform DNS in a single periodic unit cell that is the same for any other one in an array.

The (dimensionless) average velocity in each phase from the macroscopic model is directly obtained from Eq. (15), once each macroscopic term is evaluated. To do so, the solution of the closure problems given in Eqs. (A.1) and (A.2), once written in their dimensionless form, is required. To carry out this solution, the velocity field in both phases obtained from DNS was employed. Moreover, the viscosity field in the intracellular phase was pre-computed using Eq. (18) in which Γ_β^* was evaluated from the β phase velocity field resulting from DNS. In the following paragraphs, an analysis of the prediction of the macroscale velocities and the corresponding validation with DNS are presented for different values of ε_γ and viscosity ratio, μ^*.

In Fig. 11, the flow streamlines are represented for both the intracellular and extracellular fluid phases. The mean flow, despite the apparent disorder of the streamlines, goes in the horizontal (x) direction, in agreement with the horizontal macroscopic forcing applied to both phases. Here, gray objects represent large organelles, which behave as rigid solid obstacles for flow and produce deviations of the streamlines from the pressure-driven horizontal movement. Continuity of the streamlines between the intracellular and extracellular phases can be observed in this figure, in agreement with the boundary conditions stated in Section 3.3.

To analyze the influence of the volume fraction and of the rheology of the fluid phases on the average velocity in the intracellular and extracellular phases, these two parameters were considered in a variety of combinations, both in the DNS and in the prediction of the upscaled model. It must be noted that the viscosity ratios were selected based on previous reports of the viscosity values in both culture media and intracellular content, whereas the former was reported to lie in the range of 0.71×10^{-3} and 3×10^{-3} Pa s (Momen-Heravi et al., 2012; Poon, 2022; ibidi GmbH, 2022), the latter varies between 0.75×10^{-3} and 18×10^{-3} Pa s (Parker et al., 2010; Puchkov, 2013). This leads to a viscosity ratio in the range of 1 to 25 for a culture medium with a viscosity similar to water. Moreover, the Reynolds number was set to 1 in the extracellular phase, and this is motivated by the fact that, in pellets, densely populated hyphal structures do not usually allow important internal inertial momentum transport (Hille et al., 2005). In the intracellular phase, the Reynolds number was set to 0.1, slightly above the maximum reported in the literature for animal cells (Mogilner and Manhart, 2018). It is worth mentioning that, with the above set of parameters, the density ratio between the intracellular and extracellular phases is such that $0.1 \lesssim \rho_\beta/\rho_\gamma \lesssim 2.5$. In this regard, the density of cells is reported in the range of 0.75 and 1.16 g mL^{-1} (Häder et al., 2005; Itoh et al., 2021; Figueroa et al., 2022), while culture medium density is measured between 0.996 and 1.015 g mL^{-1} (Kastenhofer and Spadiut, 2020; Poon, 2022), yielding $0.65 \lesssim \rho_\beta/\rho_\gamma \lesssim 1.16$.

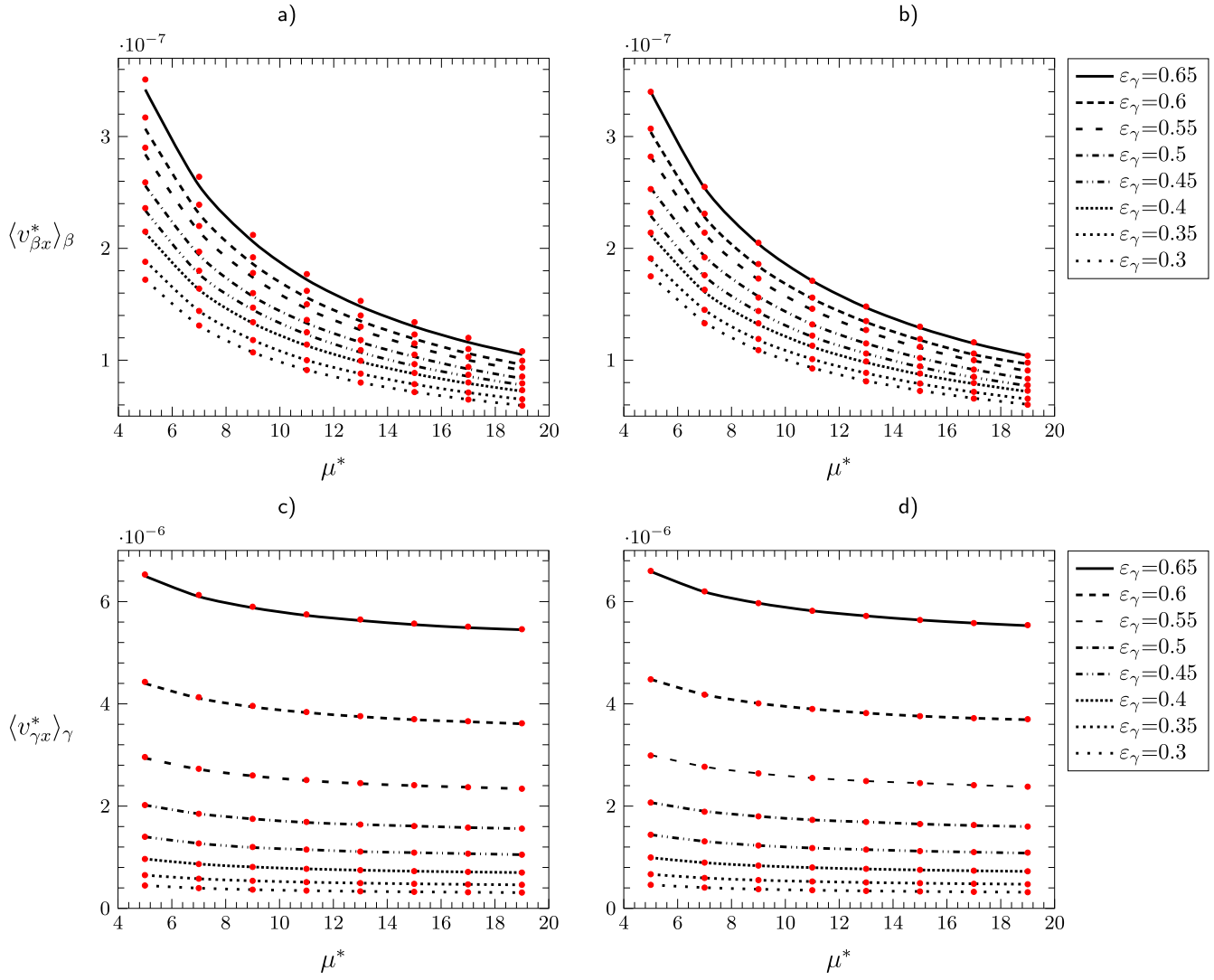

Fig. 12. Average x component of the dimensionless velocity in the intracellular ((a), (b)), $\langle v^*_{\beta x}\rangle_\beta$, or extracellular ((c), (d)), $\langle v^*_{\gamma x}\rangle_\gamma$, phase for a geometry with ((a), (c)) or without ((b), (d)) an open dolipore channel. Predictions from the macroscopic model are represented as lines whereas DNS results are plotted as red dots. Results are reported for ε_γ in the range between 0.3 and 0.65, and for $\mu^* = \mu_{ref\beta}/\mu_{ref\gamma}$ between 5 and 19, $Re_\gamma = 1$, $Re_\beta = 0.1$, $n = 1.2$ and $\lambda^* = 5$.

Results on the x component of the average dimensionless velocity, $\langle v^*_{\alpha x}\rangle_\alpha$ ($\alpha = \beta$ or γ), obtained from numerical simulations are reported in Fig. 12, for two different geometries, considering or not momentum transport between mycelial compartments. It must be noted that the absence of momentum transport between adjacent compartments, as imposed with a closed dolipore, does not imply no species transport. From these results, the following comments are in order:

- From the four graphs, (a)–(d), it is clear that the macroscopic model predictions are in excellent agreement with DNS. The relative error between the two approaches is below 5%, taking DNS as the reference, regardless the degrees of freedom investigated in all the cases reported here. This validates the macroscopic model for the velocity, indicating a correct execution of the upscaling process. It is worth mentioning that this comparison with DNS should be regarded only as a first validation step (which assesses the pertinence of the upscaling assumptions) and encourages further validation with laboratory experiments to analyze the pertinence of the starting assumptions. It must be recognized that the latter poses a problem due to the difficulty to measure the fluid velocity at the level of a single fungal cell or of a representative elementary volume portion, both in the intracellular and extracellular phases.
- The x component of the dimensionless average velocities in both the intracellular and extracellular fluid phases, respectively $\langle v^*_{\beta x}\rangle_\beta$ and $\langle v^*_{\gamma x}\rangle_\gamma$, increase with the extracellular volume fraction, ε_γ. Moreover, this effect is more pronounced as ε_γ increases.
- The x component of the dimensionless average intracellular velocity remains almost unchanged for an open (Fig. 12(a)), or closed dolipore channel (Fig. 12(b)) regardless the values of the extracellular phase volume fraction or the viscosity ratio under consideration here. This is also true for the extracellular fluid phase (see Fig. 12(c) for the open dolipore channel and 12(d) for the closed dolipore channel).
- The x component of the dimensionless average velocity in the extracellular phase is always larger (by roughly one order of magnitude) than that in the intracellular phase.

An interesting advantage of the upscaled momentum transport model implemented here is the possibility of evaluating the relative contribution from each of the terms involved in the expression of the

Table 2
Contribution from each term of the macroscopic flow model to the prediction of the average velocity for different extracellular fluid volume fractions, ε_γ, and viscosity ratios, $\mu^* = \mu_{ref\beta}/\mu_{ref\gamma}$.

	Open dolipore channel				Closed dolipore channel			
	$\varepsilon_\gamma = 0.3$ $\mu^* = 5$	$\varepsilon_\gamma = 0.65$ $\mu^* = 5$	$\varepsilon_\gamma = 0.3$ $\mu^* = 19$	$\varepsilon_\gamma = 0.65$ $\mu^* = 19$	$\varepsilon_\gamma = 0.3$ $\mu^* = 5$	$\varepsilon_\gamma = 0.65$ $\mu^* = 5$	$\varepsilon_\gamma = 0.3$ $\mu^* = 19$	$\varepsilon_\gamma = 0.65$ $\mu^* = 19$
$\langle v^*_{\beta x}\rangle_\beta$	1.72×10^{-7}	3.42×10^{-7}	5.95×10^{-8}	1.05×10^{-7}	1.76×10^{-7}	3.40×10^{-7}	6.05×10^{-8}	1.04×10^{-7}
Error_β (%)	0.18	2.40	0.12	2.65	0.72	0.07	0.55	0.30
$\xi^*_{\beta\beta}$	9.41×10^{-8} (54.7%)	1.02×10^{-7}	3.35×10^{-8}	3.24×10^{-8}	9.54×10^{-8}	9.76×10^{-8}	3.38×10^{-8}	3.09×10^{-8}
$\xi^*_{\beta\gamma}$	7.78×10^{-8} (45.2%)	2.42×10^{-7}	2.59×10^{-8}	7.35×10^{-8}	8.05×10^{-8}	2.45×10^{-7}	2.67×10^{-8}	7.41×10^{-8}
ω^*_β	-1.64×10^{-19} ($\ll$0.1%)	-5.49×10^{-16}	7.88×10^{-21}	5.25×10^{-17}	5.30×10^{-20}	-5.15×10^{-16}	-5.74×10^{-21}	5.30×10^{-17}
$\langle v^*_{\gamma x}\rangle_\gamma$	4.47×10^{-7}	6.38×10^{-6}	3.08×10^{-7}	5.36×10^{-6}	4.60×10^{-7}	6.59×10^{-6}	3.16×10^{-7}	5.53×10^{-6}
Error_γ (%)	0.18	2.40	0.12	2.65	0.72	0.07	0.55	0.30
$\xi^*_{\gamma\gamma}$	3.70×10^{-7} (82.8%)	6.14×10^{-6}	2.83×10^{-7}	5.28×10^{-6}	3.80×10^{-7}	6.36×10^{-6}	2.89×10^{-7}	5.46×10^{-6}
$\xi^*_{\gamma\beta}$	7.72×10^{-8} (17.2%)	2.40×10^{-7}	2.57×10^{-8}	7.29×10^{-8}	8.00×10^{-8}	2.41×10^{-7}	2.65×10^{-8}	7.27×10^{-8}
ω^*_γ	8.77×10^{-20} ($\ll$0.1%)	1.17×10^{-15}	-2.64×10^{-20}	-1.12×10^{-16}	6.45×10^{-19}	1.31×10^{-15}	-4.20×10^{-20}	-1.16×10^{-16}

The error % is defined as $\text{Error}_\alpha(\%) = 100\times|\langle v_{\alpha x}\rangle_{aDNS} - \langle v_{\alpha x}\rangle_a|/\langle v_{\alpha x}\rangle_{aDNS}$. Here, $\xi^*_{\alpha\alpha}$ and $\xi^*_{\alpha\kappa}$ stand, respectively, for the x-component of the dominant and coupling Darcy-like terms. Also, ω^*_α stands for the x-component of the interfacial term accounting for inertial effects. $Re_\gamma = 1$, $Re_\beta = 0.1$, $n = 1.2$ and $\lambda^* = 5$.

average velocity, and therefore, to identify the major ones and those which may be negligible. In Table 2, the contribution from each of the terms of the macroscopic momentum balance equations are reported for both the intracellular and extracellular phases. These results are presented for both open and closed dolipore channel configurations, two values of the volume fraction of the extracellular phase, $\varepsilon_\gamma = 0.3$ and 0.65, and two viscosity ratios, $\mu^* = 5$ and 19. From Table 2, the following remarks can be drawn:

1. In all cases under consideration, the major contributions are from the Darcy-like (dominant and coupling) terms of the macroscopic momentum equations as they represent together about 99% of the average velocity.
2. In the intracellular (β) phase, both Darcy-like terms are equally predominant. For the extracellular (γ) phase, the coupling term is roughly one order of magnitude smaller than that involving the dominant permeability (corresponding to viscous effects in this phase) and represents between 82 and 98% of $\langle v_{\gamma x}\rangle_\gamma$.
3. The interfacial term, in the present case, does not substantially contribute to the average velocity (its contribution is much less than 0.1%). This is attributed to the small values of the Reynolds numbers used in this work, in particular in the homogeneous core of the mycelial pellet. It is expected for the inertial contribution to play a more relevant role in the zone outside of the core (hyphal projections), where the Reynolds number usually takes larger values (Hille et al., 2005).

Since, for the structure and flow conditions considered in this work, the interfacial inertial term can be neglected in the upscaled model, the remaining Darcy-like terms could certainly be merged (since the macroscopic pressure gradients are equal), so that Eq. (10) reduces to ($\alpha, \kappa = \beta, \gamma,\ \alpha \neq \kappa$)

$$\langle \mathbf{v}_\alpha\rangle_\alpha = -\left(\frac{\mathbf{H}_{\alpha\alpha}}{\mu_{ref\alpha}} + \frac{\mathbf{H}_{\alpha\kappa}}{\mu_{ref\kappa}}\right)\cdot\nabla\langle p\rangle. \tag{19}$$

Here, $\nabla\langle p\rangle$ represents the modified pressure gradient within either the β or the γ phase. Evidently, the above model is mathematically similar to Darcy's law, with a modified apparent permeability instead of the intrinsic permeability. This raises the question of using a much simpler model with flow only in the extracellular phase, so that the cellular region is treated as a rigid impervious solid phase. This approximation is proposed since (as seen in Fig. 11 and Table 2) the extracellular phase velocity is, in most cases, one order of magnitude larger than that of the intracellular phase. With this approach, the average velocity in the extracellular phase, considering a creeping ($Re_\gamma = 0$) and Newtonian ($\mu_{ref\gamma} = \mu_\gamma$) flow, is given by the following macroscopic equation

$$\langle \mathbf{v}_\gamma\rangle_{\gamma Darcy} = -\frac{\mathbf{K}_\gamma}{\mu_\gamma}\cdot\nabla\langle p\rangle, \tag{20}$$

where $\mathbf{K}_\gamma$ is the intrinsic permeability tensor of the porous structure where the solid (rigid) skeleton is the cellular phase. The intrinsic permeability tensor is obtained from the solution of the following closure problem defined in a periodic unit cell and reported in Appendix A.2.

To evaluate the pertinence of the latter approach, the prediction of the average velocity in the extracellular phase was computed from both the single-phase Darcy model (Eq. (20)) and the complete two-phase flow macroscopic model derived here (Eq. (15), $\alpha = \gamma,\ \kappa = \beta$). This was performed with the following parameters for the modified Darcy model: $Re_\gamma = 1$, $Re_\beta = 0.1$, $n = 1.2$ and $\lambda^* = 5$, with different values of μ^* and ε_γ and for the two dolipore configurations, while, for the classical Darcy model, the only variable was ε_γ. The relative difference between the two x-components of the average velocity, taking the velocity obtained from the modified Darcy approach as the reference, is reported in Fig. 13. It can be seen that only for the largest values of the viscosity ratio, μ^*, and smaller volume fractions of the extracellular phase, ε_γ, the two approaches differ by about 6%. This is indeed expected since, in these situations where the intracellular phase occupies a large part of the unit cell and is much more viscous than the γ phase, it seems reasonable to consider that the β phase behaves as a solid. In all the other situations the difference increases up to 47%. This is true both for the open and closed dolipore channel configurations, with a slightly larger relative difference in the latter case. These results highlight the pertinence of the two-phase flow model derived in this work and the role of viscous coupling, in particular, for the prediction of momentum transport in the extracellular phase.

Finally, it must be mentioned that all the above analyses were performed with the upscaled model in its dimensionless form. However, with knowledge of the flow characteristics, (namely, viscosity and density of both phases and pressure gradient) as well as morphological properties of the structure (essentially, the curvature of the mycelial compartment), dimensional values of the macroscopic velocities can be evaluated for a particular system configuration.

4. Conclusions

In this work, total mass and momentum transport in fungal pellets were theoretically studied under an effective-medium approach. A model originally designed for porous media was adapted and implemented to fungal pellets. The governing equations at the microscale consider the steady and incompressible flow of two non-Newtonian fluids, separated by an interface. This implies regarding the cell membrane and wall as a dividing surface with structural resistance to momentum transport. In addition, organelles are assumed to be impervious to momentum transport and are thus modeled as solid phases. Moreover, the model statement is versatile in the sense that it allows considering the

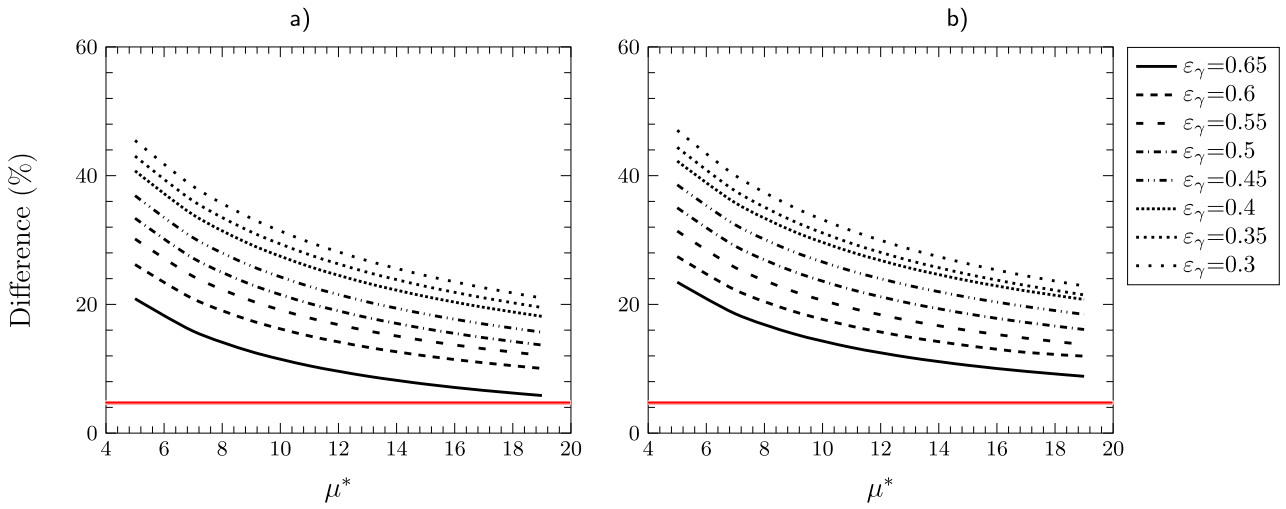

Fig. 13. Comparison in the predictions of the x-component of the average velocity in the extracellular (γ) phase from the upscaled model derived in this work (modified Darcy) and from the classical Darcy model. Results are reported for a periodic unit cell (a) considering flow between hyphal compartments (*i.e.*, an open dolipore channel) and (b) without considering flow between compartments (*i.e.*, a closed dolipore channel). The difference percentage is defined as $100\times|\langle v_{\gamma x}\rangle_{\gamma Darcy}-\langle v_{\gamma x}\rangle_\gamma|/\langle v_{\gamma x}\rangle_\gamma$ where $\langle v_{\gamma x}\rangle_\gamma$ and $\langle v_{\gamma x}\rangle_{\gamma Darcy}$ are respectively given by Eqs. (15) and (20). Results are reported for ε_γ in the range between 0.3 and 0.65 for both models, and for $\mu^*=\mu_{ref\beta}/\mu_{ref\gamma}$ between 5 and 19 for the modified Darcy model. For the latter, the following parameters were used: $Re_\gamma=1$, $Re_\beta=0.1$. The red line indicates a 5% difference threshold.

dolipore channels to be either open or closed. The resulting upscaled momentum balance equations (see Eqs. (10)) comprise four terms namely: two Darcy-like terms (a dominant one and a coupling one), as well as two interfacial terms accounting for mechanical resistance and inertial effects. The effective-medium coefficients in these equations can be predicted from the solution of two adjoint closure problems in representative periodic unit cells.

The application of the macroscopic model is restricted to homogeneous zones of fungal pellets, which were experimentally identified through microscopic examination of pellets sections of *L. trichodermophora* as an illustrative example. The geometrical characteristics of the system required to construct the unit cell for the closure problems solution were acquired using confocal and electron microscopy. Although the unit cells were specifically constructed for *L. trichodermophora*, there are certainly other fungal species that possess similar topological characteristics, which bestows some generality to the numerical simulations reported here. The macroscopic momentum balance equations were validated with direct numerical simulations, yielding less than 5% of error in all cases under study. Regardless the presence or absence of an open dolipore channel, the predicted macroscopic velocity in both the intracellular and extracellular phases was concluded to remain unaltered. This means that the dolipore configuration is unimportant in macroscopic momentum transport. Under the set of parameters considered here, the numerical results showed that the interfacial inertial term of the upscaled model did not play a significant role and thus was neglected with respect to the Darcy-like terms. This leads to a model having a mathematical structure resembling classical Darcy's law (see Eq. (19)). Though mathematically similar in structure, the predictions of the macroscopic velocity in the extracellular phase from the two approaches were found to produce significantly different results (of up to 47%). This leads to the conclusion that classical Darcy's law is not adequate, in general, to model momentum transport in fungal pellets and that the modified Darcy-like model derived here should be used instead, specially when the hyphae occupy more than 35% of the pellet volume and/or the intracellular phase is much less viscous than the extracellular phase.

As a final note, it is worth recalling that the application of the macroscale model proposed here is bounded by the associated assumptions adopted both in the statement of the microscale model and through the upscaling process. Certainly, there are many biological systems of interest that are compatible with these assumptions. These and other extensions of the derivations will be addressed in future works. In addition, the results presented here form the basis for studying both momentum transport at the hyphal projections and mass transport of species at the pellet core.

CRediT authorship contribution statement

J. Sánchez-Vargas: Writing – review & editing, Writing – original draft, Visualization, Software, Methodology, Investigation, Formal analysis, Project administration, Conceptualization. **F.J. Valdés-Parada:** Writing – review & editing, Writing – original draft, Supervision, Resources, Methodology, Investigation, Software, Conceptualization. **L. Peraza-Reyes:** Writing – review & editing, Resources, Methodology, Investigation. **D. Lasseux:** Writing – review & editing, Methodology. **M.A. Trujillo-Roldán:** Writing – review & editing, Supervision, Resources, Project administration, Funding acquisition, Conceptualization.

Declaration of competing interest

The authors have no relevant financial or non-financial interests to disclose.

Acknowledgments

J. Sánchez-Vargas is a student in Programa de Doctorado en Ciencias Bioquímicas of Universidad Nacional Autónoma de México (UNAM) and this article is part of her PhD productivity. J. Sánchez-Vargas is grateful to Consejo Nacional de Humanidades, Ciencias *y* Tecnologías (CONAHCyT) for providing her PhD scholarship (no. 802319). M.A. Trujillo-Roldán thanks the sabbatical "Programa de Apoyos para la Superación del Personal Académico" PASPA-DGAPA-UNAM. The authors are thankful to Dr. Pedro Medina Granados for the materials and technical help provided during sample preparation and sectioning for optical and electron microscopy. Also, the authors thank Dr. Guadalupe Trinidad Zavala Padilla and Dr. Miguel Tapia Rodríguez for the support during image acquisition. Finally, the authors recognize the relevant discussions about fungal biology with Dr. Roberto Garibay Orijel. This manuscript was developed under the Institutional Program of the Instituto de Investigaciones Biomédicas UNAM: "La producción de biomoléculas de interés biomédico en bacterias *y* hongos".

Funding

This work was supported by "Programa de Apoyo a Proyectos de Investigación e Innovación Tecnológica, Universidad Nacional Autónoma de México" (PAPIIT-UNAM, IN211422, IV201220). Also, this work was supported by Consejo Nacional de Humanidades, Ciencias y Tecnologías (CONAHCyT, grant CF-2023-I-1248). The funders had no role decision during publishing or preparation of the manuscript.

Appendix A

A.1. Modified Darcy closure problems

The closure (or adjoint) problems that arise during the derivation of the upscaled model for momentum transport in both the extracellular and intracellular phases (Section 3.3) can be written as follows (see details in Sánchez-Vargas et al. (2023)) ($\alpha = \beta, \gamma$)

Problem I.

$$\nabla \cdot \mathbf{D}_{\alpha\beta} = \mathbf{0}, \quad \text{in } \mathscr{V}_\alpha, \tag{A.1a}$$

$$-\frac{\rho_\alpha}{\mu_{ref\alpha}}\mathbf{v}_\alpha \cdot \nabla \mathbf{D}_{\alpha\beta} = \nabla \cdot \mathbf{T}_{\mathbf{d}_{\alpha\beta}} + \delta^K_{\alpha\beta}\mathbf{I}, \quad \text{in } \mathscr{V}_\alpha, \tag{A.1b}$$

$$\mathbf{n}_{\beta\gamma} \cdot \mu_{ref\beta}\mathbf{T}_{\mathbf{d}_{\beta\beta}} = \mathbf{n}_{\beta\gamma} \cdot \mu_{ref\gamma}\mathbf{T}_{\mathbf{d}_{\gamma\beta}}, \quad \text{at } \mathscr{A}_{\beta\gamma}, \tag{A.1c}$$

$$\mathbf{D}_{\beta\beta} = \mathbf{D}_{\gamma\beta}, \quad \text{at } \mathscr{A}_{\beta\gamma}, \tag{A.1d}$$

$$\mathbf{D}_{\beta\beta} = \mathbf{0}, \quad \text{at } \mathscr{A}_{\beta\sigma} \text{ and } \mathscr{A}_{\beta s}, \tag{A.1e}$$

$$\mathbf{D}_{\beta\beta}(\mathbf{r}) = \mathbf{D}_{\beta\beta}(\mathbf{r} + \mathbf{l}_f), \quad \text{at } \mathscr{A}_{\beta f}, \tag{A.1f}$$

$$\psi(\mathbf{r} + \mathbf{l}_i) = \psi(\mathbf{r}), \quad i = 1, 2, 3; \ \psi = \mathbf{D}_{\alpha\beta}, \mathbf{d}_{\alpha\beta}, \tag{A.1g}$$

$$\mathbf{d}_{\alpha\beta} = \mathbf{0}, \quad \text{at } \mathbf{r}^0_\alpha. \tag{A.1h}$$

Problem II.

$$\nabla \cdot \mathbf{D}_{\alpha\gamma} = \mathbf{0}, \quad \text{in } \mathscr{V}_\alpha, \tag{A.2a}$$

$$-\frac{\rho_\alpha}{\mu_{ref\alpha}}\mathbf{v}_\alpha \cdot \nabla \mathbf{D}_{\alpha\gamma} = \nabla \cdot \mathbf{T}_{\mathbf{d}_{\alpha\gamma}} + \delta^K_{\alpha\gamma}\mathbf{I}, \quad \text{in } \mathscr{V}_\alpha, \tag{A.2b}$$

$$\mathbf{n}_{\beta\gamma} \cdot \mu_{ref\beta}\mathbf{T}_{\mathbf{d}_{\beta\gamma}} = \mathbf{n}_{\beta\gamma} \cdot \mu_{ref\gamma}\mathbf{T}_{\mathbf{d}_{\gamma\gamma}}, \quad \text{at } \mathscr{A}_{\beta\gamma}, \tag{A.2c}$$

$$\mathbf{D}_{\beta\gamma} = \mathbf{D}_{\gamma\gamma}, \quad \text{at } \mathscr{A}_{\beta\gamma}, \tag{A.2d}$$

$$\mathbf{D}_{\beta\gamma} = \mathbf{0}, \quad \text{at } \mathscr{A}_{\beta\sigma} \text{ and } \mathscr{A}_{\beta s}, \tag{A.2e}$$

$$\mathbf{D}_{\beta\gamma}(\mathbf{r}) = \mathbf{D}_{\beta\gamma}(\mathbf{r} + \mathbf{l}_f), \quad \text{at } \mathscr{A}_{\beta f}, \tag{A.2f}$$

$$\psi(\mathbf{r} + \mathbf{l}_i) = \psi(\mathbf{r}), \quad i = 1, 2, 3; \ \psi = \mathbf{D}_{\alpha\gamma}, \mathbf{d}_{\alpha\gamma}, \tag{A.2g}$$

$$\mathbf{d}_{\alpha\gamma} = \mathbf{0}, \quad \text{at } \mathbf{r}^0_\alpha. \tag{A.2h}$$

Note that these problems only differ by the location of the source term, which lies within the intracellular fluid phase in Problem I and in the extracellular fluid phase in Problem II, as indicated by the use of the Kronecker delta, $\delta^K_{\alpha\kappa}$. In these problems, the following stress-like third-order tensor was used ($\alpha, \kappa = \beta, \gamma$)

$$\mathbf{T}_{\mathbf{d}_{\alpha\kappa}} = -\mathbf{I}\mathbf{d}_{\alpha\kappa} + \frac{\mu(\Gamma_\alpha)}{\mu_{ref\alpha}}\left(\nabla \mathbf{D}_{\alpha\kappa} + \nabla \mathbf{D}^{T1}_{\alpha\kappa}\right), \tag{A.3}$$

Here, $\mathbf{I}$ is the identity tensor and the superscript $T1$ denotes the transpose of a third-order tensor, which permutes the first two indices, *i.e.*, $(\nabla \mathbf{B})^{T1}_{ijk} = (\nabla \mathbf{B})_{jik}$. Similarly to the microscale problem, the boundary conditions given by Eqs. (A.1h) and (A.2h) are needed in order for the closure problem to be well posed. In these equations, $\mathbf{r}^0_\alpha$ locates an arbitrary point in the α phase.

A.2. Classical Darcy closure problem

The closure problem required to compute the intrinsic permeability tensor is reported in Whitaker (1999, Chap. 4). It is given by

$$\nabla \cdot \mathbf{D}_\gamma = \mathbf{0}, \quad \text{in } \mathscr{V}_\gamma, \tag{A.4a}$$

$$\mathbf{0} = \nabla \cdot \mathbf{T}_{\mathbf{d}_\gamma} + \mathbf{I}, \quad \text{in } \mathscr{V}_\gamma, \tag{A.4b}$$

$$\mathbf{D}_\gamma = \mathbf{0}, \quad \text{at } \mathscr{A}_{\beta\gamma}, \tag{A.4c}$$

$$\psi(\mathbf{r} + \mathbf{l}_i) = \psi(\mathbf{r}), \quad i = 1, 2, 3; \ \psi = \mathbf{D}_\gamma, \mathbf{d}_\gamma, \tag{A.4d}$$

$$\mathbf{d}_\gamma = \mathbf{0}, \quad \text{at } \mathbf{r}^0_\alpha, \tag{A.4e}$$

$$\mathbf{K}_\gamma = \langle \mathbf{D}_\gamma \rangle_\gamma. \tag{A.4f}$$

It must be noted that this problem is only defined in the extracellular phase. This is in contrast with Problems I and II from Appendix A.1 that are defined in each phase, hence composing a two-phase flow problem.

Appendix B. Supplementary data

Supplementary material related to this article can be found online at https://doi.org/10.1016/j.jtbi.2024.111853.

References

Ahmed, W.W., Fodor, É., Almonacid, M., Bussonnier, M., Verlhac, M.-H., Gov, N., Visco, P., van Wijland, F., Betz, T., 2018. Active mechanics reveal molecular-scale force kinetics in living oocytes. Biophys. J. 114 (7), 1667–1679.

Airiau, C., Bottaro, A., 2020. Flow of shear-thinning fluids through porous media. Adv. Water Resour. 143, 103658.

Amoo, L.M., Fagbenle, R.L., 2020. Overview of non-Newtonian boundary layer flows and heat transfer. In: Applications of heat, mass and fluid boundary layers. Elsevier, pp. 413–435.

Ángeles-Argáiz, R.E., Carmona-Reyes, I.A., Quintero-Corrales, C.A., Medina-Macías, F.J., Blancas-Cabrera, A., Valdez-Cruz, N.A., Ulloa, M., Trujillo-Roldán, M.A., Garibay-Orijel, R., 2020. From field sampling to pneumatic bioreactor mycelia production of the ectomycorrhizal mushroom *Laccaria trichodermophora*. Fungal Biol. 124 (3–4), 205–218.

Antonio-Rubio, N.R., Villagrán-SantaCruz, M., Santos-Vázquez, A., Moreno-Mendoza, N., 2015. Gonadal morphogenesis and sex differentiation in the oviparous lizard, *Sceloporus aeneus* (Squamata: Phrynosomatidae). Zoomorphology 134, 279–289.

Auriault, J., 1986. Remarques sur la loi de Darcy pour les écoulements biphasiques en milieu poreux. J. Méc. Théor. Appl. 141–153.

Auriault, J.-L., Boutin, C., Geindreau, C., 2009. Homogenization of coupled phenomena in heterogenous media. ISTE & Wiley.

Bartnicki-Garcia, S., Hergert, F., Gierz, G., 1989. Computer simulation of fungal morphogenesis and the mathematical basis for hyphal (tip) growth. Protoplasma 153 (1–2), 46–57.

Battiato, I., Ferrero V, P.T., Malley, D.O., Miller, C.T., Takhar, P.S., Valdés-Parada, F.J., Wood, B.D., 2019. Theory and applications of macroscale models in porous media. Transp. Porous Media 130 (1), 5–76.

Bear, J., 2018. Modeling phenomena of flow and transport in porous media. Springer, p. 767.

Bird, R.B., Stewart, W.E., Lightfoot, E.N., 2002. Transport phenomena, second ed. John Wiley, New York.

Bliatsiou, C., Schrinner, K., Waldherr, P., Tesche, S., Böhm, L., Kraume, M., Krull, R., 2020. Rheological characteristics of filamentous cultivation broths and suitable model fluids. Biochem. Eng. J. 163, 107746.

Böl, M., Schrinner, K., Tesche, S., Krull, R., 2020. Challenges of influencing cellular morphology by morphology engineering techniques and mechanical induced stress on filamentous pellet systems—A critical review. Eng. Life Sci. 21 (3–4), 51–67.

Boswell, G., 2003. Growth and function of fungal mycelia in heterogeneous environments. Bull. Math. Biol. 65 (3), 447–477.

Bottaro, A., 2019. Flow over natural or engineered surfaces: an adjoint homogenization perspective. J. Fluid Mech. 877.

Celler, K., Picioreanu, C., van Loosdrecht, M.C.M., van Wezel, G.P., 2012. Structured morphological modeling as a framework for rational strain design of *Streptomyces* species. Antonie Leeuwenhoek 102 (3), 409–423.

Charras, G.T., Coughlin, M., Mitchison, T.J., Mahadevan, L., 2008. Life and times of a cellular bleb. Biophys. J. 94 (5), 1836–1853.

Cui, Y., van der Lans, R., Giuseppin, M., Luyben, K., 1998a. Influence of fermentation conditions and scale on the submerged fermentation of *Aspergillus awamori*. Enzyme Microb. Technol. 23 (1–2), 157–167.

Cui, Y.Q., Okkerse, W.J., van der Lans, R.G.J.M., Luyben, K.C.A.M., 1998b. Modeling and measurements of fungal growth and morphology in submerged fermentations. Biotechnol. Bioeng. 60 (2), 216–229.

Das, S., Deen, N., Kuipers, J., 2018. Multiscale modeling of fixed-bed reactors with porous (open-cell foam) non-spherical particles: Hydrodynamics. Chem. Eng. J. 334, 741–759.

Davidson, F., 1998. Modelling the qualitative response of fungal mycelia to heterogeneous environments. J. Theoret. Biol. 195 (3), 281–292.
Davidson, F.A., 2007. Mathematical modelling of mycelia: a question of scale. Fungal Biol. Rev. 21 (1), 30–41.
Duarte, P.F.M., 2009. Estudos sobre o crescimento e a viabilidade de fungos ectomicorrízicos em cultivo submerso (Ph.D. thesis). Universidade Federal de Santa Catarina, URL http://repositorio.ufsc.br/xmlui/handle/123456789/93164.
El-Gendi, H., Saleh, A.K., Badierah, R., Redwan, E.M., El-Maradny, Y.A., El-Fakharany, E.M., 2021. A comprehensive insight into fungal enzymes: Structure, classification, and their role in Mankind's challenges. J. Fungi 8 (1), 23.
Espinosa-Ortiz, E.J., Rene, E.R., Pakshirajan, K., van Hullebusch, E.D., Lens, P.N., 2016. Fungal pelleted reactors in wastewater treatment: Applications and perspectives. Chem. Eng. J. 283, 553–571.
Figueroa, B., Xu, F.X., Hu, R., Men, S., Fu, D., 2022. Quantitative imaging of intracellular density with ratiometric stimulated Raman scattering microscopy. J. Phys. Chem. B 126 (39), 7595–7603.
Gamboa-Suasnavart, R.A., Valdez-Cruz, N.A., Cordova-Dávalos, L.E., Martínez-Sotelo, J.A., Servín-González, L., Espitia, C., Trujillo-Roldán, M.A., 2011. The *O*-mannosylation and production of recombinant APA (45/47 KDa) protein from *Mycobacterium tuberculosis* in *Streptomyces lividans* is affected by culture conditions in shake flasks. Microb. Cell Fact. 10 (1), 110.
Gierz, G., Bertnicki-Garcia, S., 2001. A three-dimensional model of fungal morphogenesis based on the vesicle supply center concept. J. Theoret. Biol. 208 (2), 151–164.
Gow, N.A.R., Lenardon, M.D., 2022. Architecture of the dynamic fungal cell wall. Nat. Rev. Microbiol. 21 (4), 248–259.
Gray, W.G., 1975. A derivation of the equations for multi-phase transport. Chem. Eng. Sci. 30 (2), 229–233.
Häder, D.-P., Hemmersbach, R., Lebert, M., 2005. Gravity and the Behavior of Unicellular Organisms, vol. 40, Cambridge University Press.
Hellendoorn, L., Mulder, H., van den Heuvel, J.C., Ottengraf, S.P.P., 1998. Intrinsic kinetic parameters of the pellet forming fungus *Aspergillus awamori*. Biotechnol. Bioeng. 58 (5), 478–485.
Hille, A., Neu, T., Hempel, D., Horn, H., 2005. Oxygen profiles and biomass distribution in biopellets of *Aspergillus niger*. Biotechnol. Bioeng. 92 (5), 614–623.
Hille, A., Neu, T., Hempel, D., Horn, H., 2009. Effective diffusivities and mass fluxes in fungal biopellets. Biotechnol. Bioeng. 103 (6), 1202–1213.
Howes, F.A., Whitaker, S., 1985. The spatial averaging theorem revisited. Chem. Eng. Sci. 40 (8), 1387–1392.
ibidi GmbH, 2022. Application note 11: Shear stress and shear rates for ibidi μ-slides based on numerical calculations. Techreport, ibidi GmbH, URL https://ibidi.com/img/cms/support/AN/AN11_Shear_stress.pdf, Version 6.1.
Itoh, Y., Itoh, S., Naruse, H., Kagioka, T., Hue, M.T., Abe, M., Hayashi, M., 2021. Intracellular density is a novel indicator of differentiation stages of murine osteoblast lineage cells. J. Cell. Biochem. 122 (12), 1805–1816.
Kastenhofer, J., Spadiut, O., 2020. Culture medium density as a simple monitoring tool for cell integrity of *Escherichia coli*. J. Biotechnol. 324, 100017.
Kelly, S., Grimm, L., Bendig, C., Hempel, D., Krull, R., 2006. Effects of fluid dynamic induced shear stress on fungal growth and morphology. Process Biochem. 41 (10), 2113–2117.
Keren, K., Yam, P.T., Kinkhabwala, A., Mogilner, A., Theriot, J.A., 2009. Intracellular fluid flow in rapidly moving cells. Nature Cell Biol. 11 (10), 1219–1224.
King, R., 2015. A framework for an organelle-based mathematical modeling of hyphae. Fungal Biol. Biotechnol. 2 (1).
Krull, R., Cordes, C., Horn, H., Kampen, I., Kwade, A., Neu, T.R., Nörtemann, B., 2010. Morphology of filamentous fungi: Linking cellular biology to process engineering using *Aspergillus niger*. In: Biosystems engineering II. Springer Berlin Heidelberg, pp. 1–21.
Kulkarni, K., Moon, J., Zhang, L., Lucia, A., Linninger, A.A., 2008. Multiscale modeling and solution multiplicity in catalytic pellet reactors. Ind. Eng. Chem. Res. 47 (22), 8572–8581.
Lasseux, D., Valdés-Parada, F.J., 2022. A macroscopic model for immiscible two-phase flow in porous media. J. Fluid Mech. 944, A43.
Lasseux, D., Valdés-Parada, F.J., 2023. Upscaled dynamic capillary pressure for two-phase flow in porous media. J. Fluid Mech. 959, R2.
Legorreta-Castañeda, A., Lucho-Constantino, C., Beltrán-Hernández, R., Coronel-Olivares, C., Vázquez-Rodríguez, G., 2020. Biosorption of water pollutants by fungal pellets. Water 12 (4), 1155.
Lejeune, R., Baron, G.V., 1997. Simulation of growth of a filamentous fungus in 3 dimensions. Biotechnol. Bioeng. 53 (2), 139–150.
Li, L., Liang, T., Liu, W., Liu, Y., Ma, F., 2020. A comprehensive review of the mycelial pellet: Research status, applications, and future prospects. Ind. Eng. Chem. Res. 59 (39), 16911–16922.
Mathieu, S., Manneville, J.-B., 2019. Intracellular mechanics: connecting rheology and mechanotransduction. Curr. Opin. Cell Biol. 56, 34–44.
Meyerhoff, J., Bellgardt, K.-H., 1995. A morphology-based model for fed-batch cultivations of *Penicillium chrysogenum* growing in pellet form. J. Biotechnol. 38 (3), 201–217.
Mogilner, A., Manhart, A., 2018. Intracellular fluid mechanics: Coupling cytoplasmic flow with active cytoskeletal gel. Annu. Rev. Fluid Mech. 50 (1), 347–370.
Momen-Heravi, F., Balaj, L., Alian, S., Trachtenberg, A.J., Hochberg, F.H., Skog, J., Kuo, W.P., 2012. Impact of biofluid viscosity on size and sedimentation efficiency of the isolated microvesicles. Front. Physiol. 3, 162.
Mouriño-Pérez, R.R., 2013. Septum development in filamentous ascomycetes. Fungal Biol. Rev. 27 (1), 1–9.
Nielsen, J., Krabben, P., 1995. Hyphal growth and fragmentation of *Penicillium chrysogenum* in submerged cultures. Biotechnol. Bioeng. 46 (6), 588–598.
Nolen, J., Papanicolaou, G., Pironneau, O., 2008. A framework for adaptive multiscale methods for elliptic problems. Multisc. Model. Simul. 7 (1), 171–196.
Parker, W.C., Chakraborty, N., Vrikkis, R., Elliott, G., Smith, S., Moyer, P.J., 2010. High-resolution intracellular viscosity measurement using time-dependent fluorescence anisotropy. Opt. Express 18 (16), 16607.
Patton, A.M., Marchant, R., 1978. A mathematical analysis of dolipore/parenthesome structure in basidiomycetes. J. Gen. Microbiol. 109 (2), 335–349.
Paul, G.C., Kent, C.A., Thomas, C.R., 1994. Hyphal vocuolation and fragmentation in *Penicillium chrysogenum*. Biotechnol. Bioeng. 44 (5), 655–660.
Poon, C., 2022. Measuring the density and viscosity of culture media for optimized computational fluid dynamics analysis of *in vitro* devices. J. Mech. Behav. Biomed. Mater. 126, 105024.
Pradella, J.G.C., Zuccolo, M., Lopes, S.A.R., Oliveira, M.S., 1990. *Pisolithus microcarpus* vegetative mycelia production: effects of nitrogen sources and cultivation in stirred tank fermenter. Rev. Microbiol. 22 (1), 7–11.
Puchkov, E.O., 2013. Intracellular viscosity: Methods of measurement and role in metabolism. Biochem. (Moscow) Suppl. Ser. A: Membr. Cell Biol. 7 (4), 270–279.
Raudaskoski, M., 2019. The central role of septa in the basidiomycete *Schizophyllum commune* hyphal morphogenesis. Fungal Biol. 123 (9), 638–649.
Regalado, C.M., Sleeman, B.D., 1999. Aggregation and collapse in a mechanical model of fungal tip growth. J. Math. Biol. 39 (2), 109–138.
Reyes, M.G., Beltrán-Hernánez, R., Vázquez-Rodríguez, G., Coronel-Olivares, C., Medina-Moreno, S., Juárez-Santillán, L., Lucho-Constantino, C., 2017. Formation, morphology and biotechnological applications of filamentous fungal pellets: A review. Rev. Mex. Ing. Quím. 16 (3), 703–720.
Roberson, R.W., Abril, M., Blackwell, M., Letcher, P., McLaughlin, D.J., Mouriño-Pérez, R.R., Riquelme, M., Uchida, M., 2014. Hyphal structure. In: Cellular and molecular biology of filamentous fungi. ASM Press, pp. 8–24.
Rossi, M.J., Furigo, Jr., A., Oliveira, V.L., 2007. Inoculant production of ectomycorrhizal fungi by solid and submerged fermentations. Food Technol. Biotechnol. 45 (3), 277–286, URL https://hrcak.srce.hr/24175.
Rossi, M.J., Souza, J., Oliveira, V.L., 2002. Inoculum production of the ectomycorrhizal fungus *Pisolithus microcarpus* in an airlift bioreactor. Appl. Microbiol. Biotechnol. 59 (2–3), 175–181.
Rueden, C.T., Schindelin, J., Hiner, M.C., DeZonia, B.E., Walter, A.E., Arena, E.T., Eliceiri, K.W., 2017. ImageJ2: ImageJ for the next generation of scientific image data. BMC Bioinform. 18 (1), 529.
Salejova, G., Grof, Z., Solcova, O., Schneider, P., Kosek, J., 2011. Strategy for predicting effective transport properties of complex porous structures. Comput. Chem. Eng. 35 (2), 200–211.
Sánchez-Vargas, J., Valdés-Parada, F.J., 2022. El lado matemático de la biotecnología: Un lenguaje poco entendido, pero con mucho potencial. Rev. Divulg. Cient. iBIO 4 (2), 6–9.
Sánchez-Vargas, J., Valdés-Parada, F.J., Lasseux, D., 2022. Macroscopic model for unsteady generalized Newtonian fluid flow in homogeneous porous media. J. Non-Newton. Fluid Mech. 306, 104840.
Sánchez-Vargas, J., Valdés-Parada, F.J., Trujillo-Roldán, M.A., Lasseux, D., 2023. Macroscopic model for generalised Newtonian inertial two-phase flow in porous media. J. Fluid Mech. 970, A19.
Schmideder, S., Barthel, L., Muller, H., Meyer, V., Briesen, H., 2019. From three-dimensional morphology to effective diffusivity in filamentous fungal pellets. Biotechnol. Bioeng. 116 (12), 3360–3371.
Schmideder, S., Muller, H., Barthel, L., Friedrich, T., Niessen, L., Meyer, V., Briesen, H., 2020. Universal law for diffusive mass transport through mycelial networks. Biotechnol. Bioeng. 118 (2), 930–943.
Schügerl, K., Wittler, R., Lorenz, T., 1983. The use of molds in pellet form. Trends Biotechnol. 1 (4), 120–123.
Shamlou, P.A., Makagiansar, H., Ison, A., Lilly, M., Thomas, C., 1994. Turbulent breakage of filamentous microorganisms in submerged culture in mechanically stirred bioreactors. Chem. Eng. Sci. 49 (16), 2621–2631.
Silva, E.E., Gutierrez, G., Dendooven, L., Jimenez, H., Ochoa-Tapia, J., 2001. A method to evaluate the isothermal effectiveness factor for dynamic oxygen into mycelial pellets in submerged cultures. Biotechnol. Prog. 17 (1), 95–103.
Slattery, J.C., Sagis, L., Oh, E.-S., 2006. Interfacial transport phenomena, second ed. Springer.
Stamenović, D., 2008. Rheological behavior of mammalian cells. Cell. Mol. Life Sci. 65 (22), 3592–3605.
Sumbali, G., Johri, B.M., Johrit, B.M., 2005. The fungi. Alpha Science International, Ltd, p. 312.
Tindemans, S.H., Kern, N., Mulder, B.M., 2006. The diffusive vesicle supply center model for tip growth in fungal hyphae. J. Theoret. Biol. 238 (4), 937–948.
Tough, A.J., Prosser, J.I., 1996. Experimental verification of a mathematical model for pelleted growth of *Streptomyces coelicolor* A3(2) in submerged batch culture. Microbiology 142 (3), 639–648.

Tough, A.J., Pulham, J., Prosser, J.I., 1995. A mathematical model for the growth of mycelial pellet populations. Biotechnol. Bioeng. 46 (6), 561–572.

Van Driel, K.G.A., 2007. Septal pore caps in Basidiomycetes, composition and ultrastructure (Ph.D. thesis). Utrecht University.

Van Driel, K.G.A., Van Peer, A.F., Grijpstra, J., Wosten, H.A.B., Verkleij, A.J., Muller, W.H., Boekhout, T., 2008. Septal pore cap protein SPC18, isolated from the basidiomycetous fungus *Rhizoctonia solani*, also resides in pore plugs. Eukaryotic Cell 7 (10), 1865–1873.

Van Peer, A.F., Muller, W.H., Boekhout, T., Lugones, L.G., Wösten, H.A.B., 2009. Cytoplasmic continuity revisited: Closure of septa of the filamentous fungus *Schizophyllum commune* in response to environmental conditions. In: Idnurm, A. (Ed.), PLoS ONE 4 (6), e5977.

Van Peer, A.F., Wang, F., Van Driel, K.G.A., De Jong, J.F., Van Donselaar, E.G., Muller, W.H., Boekhout, T., Lugones, L.G., Wosten, H.A.B., 2010. The septal pore cap is an organelle that functions in vegetative growth and mushroom formation of the wood-rot fungus *Schizophyllum commune*. Environ. Microbiol. 12 (4), 833–844.

Vasquez-Martínez, N., Guillén, D., Moreno-Mendieta, S.A., Medina-Granados, P., Casañas-Pimentel, R.G., San Martín-Martínez, E., Morales, M.Á., Sanchez, S., Rodríguez-Sanoja, R., 2023. *In vivo* tracing of immunostimulatory raw starch microparticles after mucosal administration. Eur. J. Pharmaceut. Biopharmaceut. 187, 96–106.

Venneman, J., Pawlick, J.S., Audenaert, K., Meyer, E., Demeyere, K., Leus, L., Baert, G., Kogel, K.-H., Haesaert, G., Vereecke, D., Ehlers, K., 2020. Evaluation of genome size and quantitative features of the dolipore septum as taxonomic predictors for the *Serendipita 'williamsii'* species complex. Fungal Biol. 124 (9), 781–800.

Vetchinkina, E., Kupryashina, M., Gorshkov, V., Ageeva, M., Gogolev, Y., Nikitina, V., 2017. Alteration in the ultrastructural morphology of mycelial hyphae and the dynamics of transcriptional activity of lytic enzyme genes during basidiomycete morphogenesis. J. Microbiol. 55 (4), 280–288.

Whitaker, S., 1986. Flow in porous media II: The governing equations for immiscible, two-phase flow. Transp. Porous Media 1 (2), 105–125.

Whitaker, S., 1999. The method of volume averaging. Springer Netherlands, Dordrecht.

Wittler, R., Baumgartl, H., Lübbers, D.W., Schügerl, K., 1986. Investigations of oxygen transfer into *Penicillium chrysogenum* pellets by microprobe measurements. Biotechnol. Bioeng. 28 (7), 1024–1036.

Wood, B.D., Whitaker, S., 1999. Cellular growth in biofilms. Biotechnol. Bioeng. 64 (6), 656–670.

Yang, H., Reichl, U., King, R., Gilles, E.D., 1992. Measurement and simulation of the morphological development of filamentous microorganisms. Biotechnol. Bioeng. 39 (1), 44–48.

Yang, X., Wang, S., Jin, H., He, Y., 2023. Pore-scale simulation of flow and mass transfer characteristics of porous particle. Chem. Eng. Sci. 267, 118301.